

Statistics

Wednesday, September 1, 2021 2:17 PM

Statistics:

How do we know something is true? Not primarily a branch of mathematics, but is a branch of philosophy.

2 Primary groups of statisticians

- Frequentists
- Bayesians

Frequentist Approach - Imagine doing your experiment a billion times - How often would you get the results like yours? (Similar to a guess and check approach)

Bayesian Approach - Based on your data, you change your degree of belief in the truth.

Poisson Distribution: $P(N | \mu) = [e^{-\mu} * \mu^N] / N!$

Where μ is the average number you would measure (not an integer)
 N is how many times you measure (an integer)

As μ and N get sufficiently large => $P(x | \mu, \sigma) = 1/\sqrt{2\pi\sigma^2} * e^{-(x-\mu)^2/2\sigma^2}$ also called the **Gaussian Distribution/Normal Distribution**

Essentially Poisson is for integral values, Gaussian is for everything else.

Bayes' Theorem ($P(B|A) * P(A) / P(B) = P(A|B)$)

In general - parameters belong to theory, and observables belong to experiments.

Going from experiments to parameters are stats.

Bayesians say that $P(B)$ is your degree of belief in different values of the parameter. But what is $P(B)$ - The prior!!

Frequentist Approach - Given a certain parameter, how likely are you to get your data?

Background: 21

Signal Expected: $20/M(\text{higgs mass})$

Observed: 21

Low M: We should have seen it

High M: We cannot tell if it's there or not.

The point in between (we didn't see it vs we cannot tell if it is there) is called the lower limit (around 95%).

What we are looking for

Wednesday, September 1, 2021 2:38 PM

1 - Doubly Charged Higgs (Does it exist?)

2 - Dark photons - Small connection between the SM and Dark SM is called 'kinetic mixing.' ()

Signal - Decays into decay products - but there are other things that also decay into the same products - called Background.

Central problem of particle physics

Example:

Background : 53

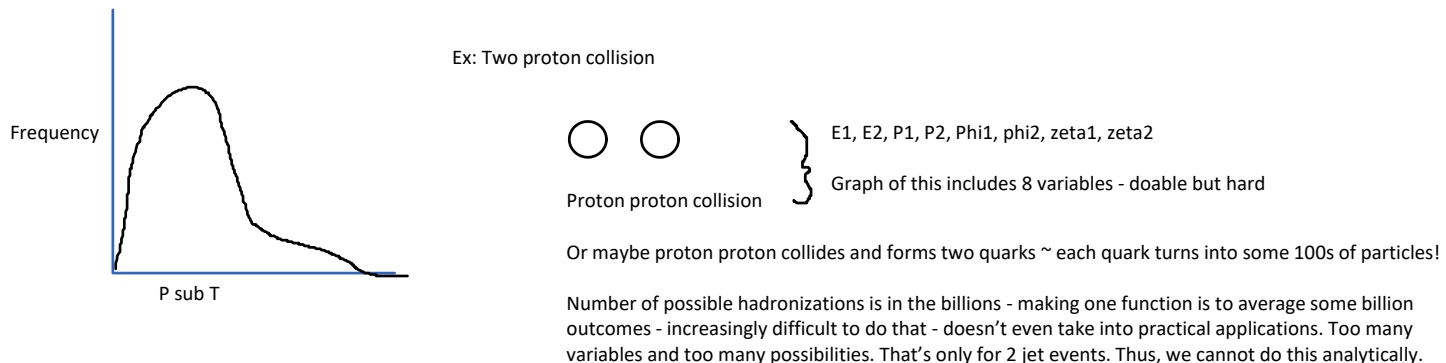
We see : 62 => 9 signal events - But background prediction is a probabilistic function so we do not know for sure.

At the end of the day, we want to find and set a limit.

Monte Carlo Simulations

Wednesday, September 22, 2021 2:10 PM

There exists a fundamental randomness with physics: For example,



Solution: Monte Carlo

Gets around this problem by random numbers. You make up simulated events using random numbers (based on theory) - that is instead of making a function, we run simulations to take an average.

Generates one event that is realistic in happening.

Methodology:

- 1) Create an 'lots' of events using random numbers. Now we have a bunch of events such that the aggregate looks like what actually happens.
- 2) Using the events to create histograms. By choosing a lot of random numbers, we get an actual statistical sample.

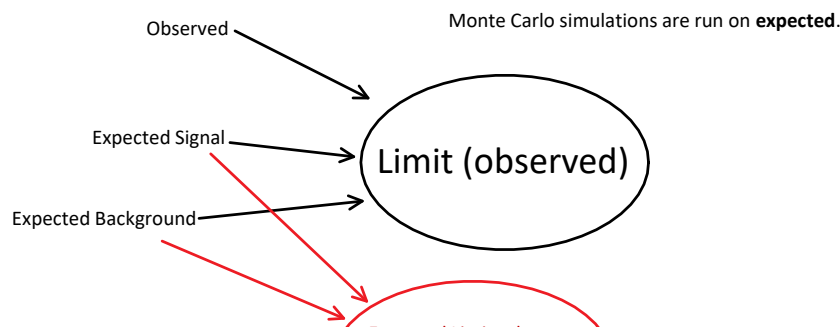
Main Problem with the Monte Carlo simulation: It is random - so technically, the answer you get changes over time. A choppy/spiky histogram means the sample size of the Monte Carlo is not accurate.

Requires a simulation of the detector - which is hard to do, since the entire structure has to model, and you have to calculate what happens to the particle as it moves through space. But this is slow, since each simulation takes a minute, and we have billions of particles.

BUT ALL OF THIS IS ALL A SIMULATION - SIMULATED DATA AND SIMULATED RESULTS.
But this tells us what we should be looking for - which the simulation tells us. Rather, it tells us what the histogram should look like.

Monte Carlo Generator - PYTHIA - having generated these events, we run them through a detector simulation (GEANT4) ----> Reconstruction (turns data and charges into physics objects [electrons, muons, photons, etc.]) -----> and we make histograms from this.

Simultaneously, we take raw data, and we can use it join in at the reconstruction level.



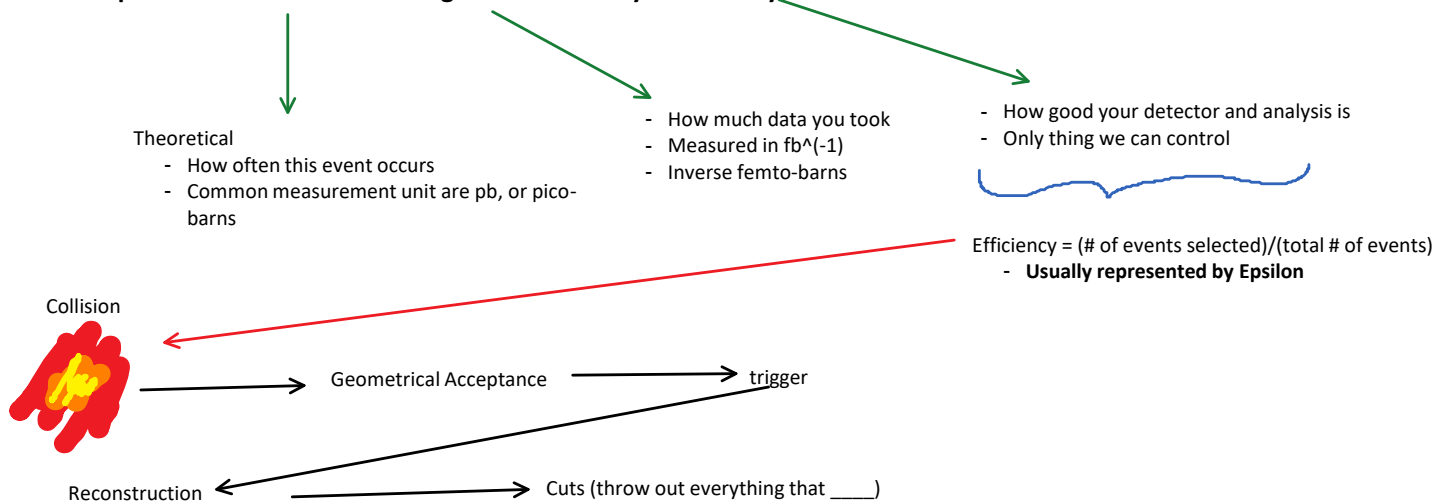
Expected Limit - the
average limit you would
get if there is no signal

Tells you about the expected sensitivity of experiment

Events

Wednesday, September 29, 2021 2:43 PM

of events expected = cross section x integrated luminosity x efficiency



So at the end of everything, efficiencies are generally in the 60%.

Epsilon_trig x Epsilon_reco x Epsilon_cuts x SF_trig x SF_reco x SF_cuts => But there are uncertainties everywhere.

All of these uncertainties are called systematic uncertainties, meaning the expected values are also having uncertainties. All of these uncertainties could be correlated or uncorrelated. Then feed the list of them (typically 12 to 15) into the Limit.

Flavors

Wednesday, October 6, 2021 2:49 PM

- One particle and its antiparticle
electron, muon, tau → compare lepton-flavor universality
(how often you get electrons vs muons)

Symmetry

Wednesday, October 6, 2021 3:31 PM

- a function $\rightarrow \mathbb{A}^x$ that output equals the input
(reflection, rotation, ...)

that is for $\sim \mathcal{L}$,

$$\mathcal{L}(f(x)) = \mathcal{L}(x)$$

CMS Dilepton Annotations

Wednesday, October 6, 2021 1:43 PM

1 Introduction

The presence of new phenomena, both resonant and nonresonant, in the high-mass dilepton final state is predicted by various theoretical models aiming to extend the standard model (SM) of particle physics. In this paper, the production of new spin-1 or spin-2 resonances, as well as the nonresonant production of high-mass lepton pairs, is considered.

The existence of new neutral gauge bosons is a possible signature of grand unified theories, such as superstring and left-right-symmetric (LRS) models, that include a unification of the three forces at a high energy scale [1, 2].

One persistent puzzle in modern particle physics is the large difference in the energy scale of electroweak symmetry breaking and the energy scale of gravitation. This could be explained in theories including spatial extra dimensions, where the gravitational force can propagate into additional dimensions. In models by Arkani-Hamed, Dimopoulos, and Dvali (ADD) [3, 4], the SM particles are confined to the traditional four dimensions of space and time, while in models proposed by Randall and Sundrum (RS) [5] the SM particles could also propagate into the additional dimensions. Possible signatures of these theories at LHC energies are graviton excitations, either as distinct spin-2 high-mass resonances in the RS model, or as a series of nearly mass-degenerate excitations that result in an overall nonresonant excess of events at high mass in the ADD model.

Based on many astrophysical and cosmological observations, it is assumed that dark matter (DM) accounts for the majority of matter in the universe [6]. Models have been proposed in which the DM consists of particles that can interact with those of the SM via high-mass, weakly coupled mediator particles [7]. These mediators could then be observed via their decay into SM particles, including the dilepton final state.

It has long been speculated that the presence of three generations of quarks and leptons is a sign that these particles are not fundamental but rather composed of constituent particles commonly called “preons” [8]. At energies observable at collider experiments, the preons would be confined into bound states by a new interaction analogous to quantum chromodynamics (QCD). This new interaction is characterized by an energy scale Λ , at which its effects would be directly observable. At center-of-mass energies far below Λ , the presence of the preon bound states would manifest itself as a flavor-diagonal “contact interaction” (CI) [9], resulting in a nonresonant excess of events at high mass.

Hints for lepton flavor universality violation in several measurements recently reported by the LHCb Collaboration [10–12], together with other flavor anomalies in B-meson decays summarized in Ref. [13], have sparked interest in models for physics beyond the SM that could explain these effects. These include models with heavy neutral gauge bosons [2] or leptoquarks [14]. Some of these models would result in a significant deviation from unity of the ratio of the dimuon to dielectron differential cross section as a function of dilepton mass $m_{\ell\ell}$,

$$R_{\mu^+\mu^-/\text{e}^+\text{e}^-} = \frac{d\sigma(q\bar{q} \rightarrow \mu^+\mu^-)/dm_{\ell\ell}}{d\sigma(q\bar{q} \rightarrow \text{e}^+\text{e}^-)/dm_{\ell\ell}}, \quad (1)$$

at high $m_{\ell\ell}$ [15].

Searches for high-mass Z' gauge bosons in dilepton final states have a long history at the LHC, with the CMS Collaboration having reported results using proton-proton (pp) collision data from the LHC Run 1 (2010–2012) at $\sqrt{s} = 7 \text{ TeV}$ [16, 17] and 8 TeV [18, 19], and more recently from the beginning of the LHC Run 2 (2015–2018) at 13 TeV [20, 21] using early data corresponding to an integrated luminosity of 36 fb^{-1} collected in 2016. Similar searches have also

been performed by the ATLAS Collaboration with data collected at 7 TeV [22, 23], 8 TeV [24], and 13 TeV [25]. Most recently, the ATLAS Collaboration reported results obtained using data recorded at $\sqrt{s} = 13$ TeV, corresponding to an integrated luminosity of 139 fb^{-1} [26].

Results of searches for spin-2 dilepton resonances, as well as constraints on DM models, have been reported by the ATLAS and CMS Collaborations [18, 21, 24, 27].

For the case of nonresonant signatures, the CMS Collaboration has reported results at 8 [19] and 13 TeV [28]. Additional constraints on these models have been reported by the CMS Collaboration from diphoton and dijet final states [29, 30] and by the ATLAS Collaboration from dijet final states [31]. The ATLAS Collaboration has presented similar results for these models in the dilepton final state, the most recent using data at 8 TeV [32] for the ADD model and at 13 TeV [33] for the CI model.

This paper significantly extends the previous CMS results by using the full data set recorded at $\sqrt{s} = 13$ TeV during the years 2016–2018, corresponding to 137 (140) fb^{-1} in the dielectron (dimuon) channel [34–36]. The additional data in the dimuon channel are recorded with the detector in conditions unsuitable for electron reconstruction. Deviations from the SM predictions are searched for in the dilepton invariant mass spectrum for both dielectron and dimuon events. The contribution from dileptonic decays of tau lepton pairs to the signal is small and neglected. The shapes of contributions from SM processes are estimated from simulation, except for backgrounds containing leptons produced inside jets or jets misidentified as leptons, which are estimated from control regions in data. The simulated events describing the dominant Drell–Yan (DY) background are corrected to the highest order calculations available. The resulting background shape is normalized to the observed data yields in a mass window of 60–120 GeV around the Z boson peak, separately for the dielectron and dimuon channels.

Two analysis strategies are followed, targeting resonant and nonresonant signatures. For resonant signatures, the search is performed in a mass window around the assumed resonance mass, whose size depends on the assumed intrinsic decay width of the resonance and the mass-dependent detector resolution. A range of masses and widths is scanned to provide results covering a wide selection of signal models. Unbinned maximum likelihood fits are performed inside the mass windows, allowing the background normalization to be determined from data. The background parametrizations are obtained from fits to the $m_{\ell\ell}$ distribution of the background estimates.

Upper limits are set on the ratio of the product of the production cross section and the branching fraction of a new narrow dilepton resonance to that of the SM Z boson. Thus, many experimental and theoretical uncertainties common to both measurements cancel out or are reduced, leaving only uncertainties in the ratio that vary with the dilepton mass to be considered.

In the case of nonresonant signatures, the event sample is divided into several bins in invariant mass and, improving upon previous CMS analyses, the scattering angle $\cos \theta^*$ in the Collins–Soper frame [37]. The result is then obtained from a combination of the individual counting experiments within these bins. While most of the sensitivity to new physics stems from the highest mass bins where the signal-to-background ratio is most favorable, the bins at lower masses still contain valuable information, for example on possible interference between the signal and SM backgrounds. In this approach, the signal is not normalized to the Z boson cross section, and the background estimate cannot be obtained from the data. Therefore, this part of the analysis is more affected by uncertainties in the signal and background modeling.

In addition to these two search strategies, lepton flavor universality is tested for the first time in these final states by measuring the dimuon to dielectron ratio $R_{\gamma\gamma\rightarrow\mu\mu/\gamma\gamma\rightarrow e\bar{e}}$ and comparing

it to the SM expectation of unity, including corrections for detector effects, lepton acceptances, and lepton efficiencies.

This paper is structured as follows. The CMS detector is briefly described in Section 2. A description of the signal models is given in Section 3, followed by a description of simulated event samples used in the analysis in Section 4. The event reconstruction and selection is given in Section 5 and the estimation of SM backgrounds is described in Section 6. Systematic uncertainties are described in Section 7, followed by the results and their statistical interpretation in Sections 8 and 9, respectively. The paper is summarized in Section 10. Tabulated results are provided in HEPDATA [38].

2 The CMS detector

The central feature of the CMS detector is a superconducting solenoid providing an axial magnetic field of 3.8 T and enclosing an inner tracker, an electromagnetic calorimeter (ECAL), and a hadron calorimeter (HCAL). The inner tracker is composed of a silicon pixel detector and a silicon strip tracker, and measures charged particle trajectories in the pseudorapidity range $|\eta| < 2.5$. Before the data taking period in 2017, an upgraded pixel detector was installed, adding an additional barrel layer closer to the interaction point and additional disks in the two forward parts of the detector [39]. The ECAL and HCAL, each composed of a barrel and two endcap sections, extend over the range $|\eta| < 3.0$. The finely segmented ECAL consists of nearly 76 000 lead tungstate crystals, while the HCAL is constructed from alternating layers of brass and scintillator. Forward hadron calorimeters encompass $3.0 < |\eta| < 5.0$. The muon detection system covers $|\eta| < 2.4$ with up to four layers of gas-ionization detectors installed outside the solenoid and sandwiched between the layers of the steel flux-return yoke. A more detailed description of the CMS detector, together with a definition of the coordinate system used and the relevant kinematic variables, can be found in Ref. [40].

Events of interest are selected using a two-tiered trigger system [41]. The first level (L1), composed of custom hardware processors, uses information from the calorimeters and muon detectors to select events at a rate of around 100 kHz within a fixed time interval of less than 4 μ s. The second level, known as the high-level trigger (HLT), consists of a farm of processors running a version of the full event reconstruction software optimized for fast processing, and reduces the event rate to around 1 kHz before data storage.

3 Signal models

A large number of models predict new phenomena resulting in high-mass dilepton signatures. The available models may be classified depending on whether they predict resonant or non-resonant production.

3.1 Models with resonant signatures

We consider three types of models resulting in resonances at high dilepton masses: Z' particles in a class of $U'(1)$ gauge group models, spin-2 gravitons in the RS model of extra dimensions, and spin-1 dark matter mediators. The most prevalent are the theories that introduce new $U'(1)$ gauge groups. The symmetry properties of these groups, or a combination of them, are broken at some energy scale so that the SM group structure emerges as the low-energy limit of the new theory. If this breaking happens at the TeV scale, new gauge bosons Z' with masses accessible at the LHC could exist. The properties of the new Z' bosons depend on the mixing

of the $U'(1)$ generators, which can be described by a continuously varying angle within a class of models. Commonly considered classes are the generalized sequential model (GSM) [42], containing the sequential SM boson Z'_{SSM} that has SM-like couplings to SM fermions [43]; LRS extensions of the SM based on the $SU(2)_L \otimes SU(2)_R \otimes U(1)_{B-L}$ gauge group, where $B-L$ refers to the difference between the baryon and lepton numbers [42], which predict high-mass neutral bosons; and grand unified theories based on the E_6 gauge group, containing the Z'_{ψ} boson [1, 44].

In the narrow width approximation [45], the Z' production cross section can be expressed as $c_u w_u + c_d w_d$, where c_u (c_d) are its couplings to up-type (down-type) quarks and w_u (w_d) are the parton distribution functions (PDFs) for these quarks [42, 46]. As the values of the model-dependent couplings depend on the aforementioned mixing of the $U'(1)$ generators, each class of models can be represented by a unique contour in the (c_d, c_u) plane as a function of the mixing angle. The properties of a variety of benchmark models in the three model classes mentioned above are shown in Table 1. Ref. [42] shows that the finite width of the resonance, which can reach up to 12% for the Z'_Q , has negligible effects on the translation of experimental limits obtained in the narrow width approximation into the (c_d, c_u) plane. Similarly, the effect of interference between the signal and SM backgrounds can be neglected as long as the signal cross section is considered in a sufficiently narrow window around the Z' mass [45].

Table 1: Various benchmark models in the GSM [42], LRS [42], and E_6 [1, 44] model classes, with their corresponding mixing angles, their branching fraction (\mathcal{B}) to dileptons, the c_u , c_d parameters and their ratio, and the width-to-mass ratio of the associated Z' boson.

$U'(1)$ model	Mixing angle	$\mathcal{B}(\ell^+ \ell^-)$	c_u	c_d	c_u/c_d	$\Gamma_{Z'}/M_{Z'}$
GSM						
$U(1)_{\text{SM}}$	-0.072π	0.031	2.43×10^{-3}	3.13×10^{-3}	0.78	0.0297
$U(1)_{\text{T3L}}$	0	0.042	6.02×10^{-3}	6.02×10^{-3}	1.00	0.0450
$U(1)_Q$	0.5π	0.125	6.42×10^{-2}	1.60×10^{-2}	4.01	0.1225
LRS						
$U(1)_R$	0	0.048	4.21×10^{-3}	4.21×10^{-3}	1.00	0.0247
$U(1)_{\text{B-L}}$	0.5π	0.154	3.02×10^{-3}	3.02×10^{-3}	1.00	0.0150
$U(1)_{\text{LR}}$	-0.128π	0.025	1.39×10^{-3}	2.44×10^{-3}	0.57	0.0207
$U(1)_Y$	0.25π	0.125	1.04×10^{-2}	3.07×10^{-3}	3.39	0.0235
E_6						
$U(1)_\chi$	0	0.061	6.46×10^{-4}	3.23×10^{-3}	0.20	0.0117
$U(1)_\psi$	0.5π	0.044	7.90×10^{-4}	7.90×10^{-4}	1.00	0.0053
$U(1)_\eta$	-0.29π	0.037	1.05×10^{-3}	6.59×10^{-4}	1.59	0.0064
$U(1)_S$	0.129π	0.066	1.18×10^{-4}	3.79×10^{-3}	0.31	0.0117
$U(1)_N$	0.42π	0.056	5.94×10^{-4}	1.48×10^{-3}	0.40	0.0064

The RS model of extra dimensions [5, 47] introduces an additional warped spatial dimension where gravity can propagate through all of the five-dimensional bulk. This leads to the prediction of spin-2 Kaluza–Klein (KK) excitations of the graviton (G_{KK}) that could be resonantly produced at the LHC and observed in their decay into lepton pairs. These new resonances are characterized by their masses and the coupling k/M_{Pl} , where k is the warp factor of the five-dimensional anti-de Sitter space and \bar{M}_{Pl} is the reduced Planck mass. The ratios of the intrinsic widths of the first excitation of the graviton to its mass for the coupling parameters k/\bar{M}_{Pl} of 0.01, 0.05, and 0.10 are 0.01%, 0.36%, and 1.42%, respectively.

To ensure a consistent search strategy and comparability between the results of different searches, the LHC Dark Matter Working Group has defined a variety of simplified models to be used as benchmarks for DM searches at the LHC [48, 49]. In this paper, we consider a model that assumes the existence of a single DM particle that interacts with the SM particles through a spin-1 mediator, which can be either a vector or axial-vector boson. The model is fully described by the following parameters: the DM mass m_{DM} , the mediator mass m_{med} , the coupling g_{DM} between the mediator and the DM particle, and the universal couplings g_ℓ and g_q between the mediator and the SM charged leptons and quarks, respectively. Two signal scenarios have been defined that feature nonzero values of g_ℓ , so that the mediator could be directly observed in its decay into the dilepton final state. The first choice represents a relative strength of the couplings to quarks and charged leptons typical of some models with a pure vector mediator, while the second choice is a representative case found in the simplest complete models with axial-vector Z' bosons [48]:

- Vector mediator with small couplings to leptons: $g_{\text{DM}} = 1.0$, $g_q = 0.1$, $g_\ell = 0.01$;
- Axial-vector mediator with equal couplings to quark and leptons: $g_{\text{DM}} = 1.0$, $g_q = g_\ell = 0.1$.

Interference between the mediator exchange and the SM processes resulting in the dilepton final state has been studied and found to be negligible for experimental searches [48].

3.2 Models with nonresonant signatures

We consider two types of nonresonant excess at high $m_{\ell\ell}$: a series of virtual spin-2 graviton excitations in the ADD model of large extra dimensions [3], and a four-fermion CI caused by fermion substructure [8]. In these models, the differential cross section for dilepton pair production can be expressed as:

$$\frac{d\sigma_{X \rightarrow \ell\ell}}{dm_{\ell\ell}} = \frac{d\sigma_{\text{DY}}}{dm_{\ell\ell}} + \eta_X \mathcal{I}(m_{\ell\ell}) + \eta_X^2 \mathcal{S}(m_{\ell\ell}), \quad (2)$$

where $d\sigma_{\text{DY}}/dm_{\ell\ell}$ is the SM DY differential cross section, η_X is a model-specific parameter, and the signal contribution terms are separated into an interference term (\mathcal{I}) and a pure signal term (\mathcal{S}). Interference between the signal process and the SM DY background is possible when the new process acts on the same initial state and yields the same final state, and can be either constructive or destructive, depending on the sign of η_X .

In the ADD model, which is an attempt to describe quantum gravity with an effective field theory, spacetime is extended by n additional compactified spatial dimensions of size L . SM particles are confined to the four-dimensional subspace (the brane), while gravity can propagate to all $D = n + 4$ dimensions (the bulk). If L is sufficiently large, the D -dimensional fundamental Planck mass M_D , which is related to the effective Planck mass M_{Pl} in three dimensions by

$$M_D^{2+n} \sim M_{\text{Pl}}^2 / L^n, \quad (3)$$

can then be probed at the TeV scale. In contrast to the RS model, the ADD model predicts the presence of a quasi-continuous spectrum of KK graviton modes as a result of the compactification of the extra dimensions with a large compactification radius. The number of excited modes increases with the interaction scale, resulting in a nonresonant excess at high dilepton masses from the decay of the virtual gravitons, which cannot be individually resolved with the LHC detectors.

These processes can be characterized by the single energy cutoff scale Λ_T in the Giudice–Rattazzi–Wells (GRW) convention [50], the string scale M_s in the Hewett convention [51], or

the number of additional dimensions n in conjunction with M_S in the Han–Lykken–Zhang (HLZ) convention [52]. The generic form factor η_X in Eq. (2) is replaced by η_G , which depends on the chosen convention:

$$\text{GRW:} \quad \eta_G = \frac{1}{\Lambda_T^4}; \quad (4)$$

$$\text{Hewett:} \quad \eta_G = \frac{2}{\pi} \frac{\lambda}{M_S^4} \quad \text{with } \lambda = \pm 1; \quad (5)$$

$$\text{HLZ:} \quad \eta_G = \begin{cases} \ln(M_S^2/\hat{s}) \frac{1}{M_S^4} & \text{for } n = 2, \\ \frac{2}{n-2} \frac{1}{M_S^4} & \text{for } n > 2. \end{cases} \quad (6)$$

Here \hat{s} is the square of the parton center-of-mass energy. In the ADD model, interference with DY is limited, as the production of virtual gravitons is dominated by gluon-induced processes. Positive interference is assumed in this analysis, but the choice has negligible effects on the results. The effective field theory will only yield reliable results up to a certain energy scale, above which a more exact theory of quantum gravity is necessary. Both Λ_T and M_S act as this ultraviolet cutoff parameter in their respective conventions.

In case of the CI model, assuming that quarks and leptons share common constituents, the Lagrangian for the CI process $q\bar{q} \rightarrow \ell\ell$, where ℓ is a charged lepton, can be expressed as

$$\mathcal{L}_{q\ell} = \frac{g_{\text{contact}}^2}{\Lambda^2} \left[\eta_{LL} (\bar{q}_L \gamma^\mu q_L) (\bar{\ell}_L \gamma_\mu \ell_L) + \eta_{RR} (\bar{q}_R \gamma^\mu q_R) (\bar{\ell}_R \gamma_\mu \ell_R) + \eta_{LR} (\bar{q}_L \gamma^\mu q_L) (\bar{\ell}_R \gamma_\mu \ell_R) + \eta_{RL} (\bar{q}_R \gamma^\mu q_R) (\bar{\ell}_L \gamma_\mu \ell_L) \right], \quad (7)$$

where $q_L = (q_u, q_d)_L$ is a left-handed quark doublet; q_R represents a sum over the right-handed quark singlets (q_u - and q_d -type); the η_{ij} are real numbers between -1 and 1 ; and ℓ_L and ℓ_R are the left- and right-handed lepton fields, respectively. By convention, $g_{\text{contact}}^2/4\pi = 1$ and the helicity parameters η_{ij} are taken to have unit magnitude. The compositeness scale, represented by Λ , is potentially different for each of the individual terms in the Lagrangian. Therefore, the individual helicity currents for “left-left” (LL), “right-right” (RR), and the combination of “left-right” (LR) and “right-left” (RL) in Eq. (7), together with their scales (Λ_{LL} , Λ_{RR} , Λ_{LR} , and Λ_{RL}), are considered separately in this search, and in each case all other currents are assumed to be zero. While the LL and RR models favor positive values of $\cos\theta^*$, as does the DY background, the distribution is inverted for the LR and RL models, which favor negative values.

A given η_{ij} can be related to the form factor in the differential cross section in Eq. (2) by

$$\eta_X = -\frac{\eta_{ij}}{\Lambda_{ij}^2}. \quad (8)$$

4 Simulated event samples

Numerous simulated event samples are used to describe both background and signal processes. Dedicated samples are generated for each of the three years of data taking considered in this analysis, reflecting the changing beam and detector conditions from year to year. Different generators are used to generate the individual processes.

The dominant DY background is generated with POWHEG v2 [53–58] using next-to-leading order (NLO) matrix elements. In the sample generation, PDFs are evaluated using the LHAPDF

Resonance and Nonresonance Signatures

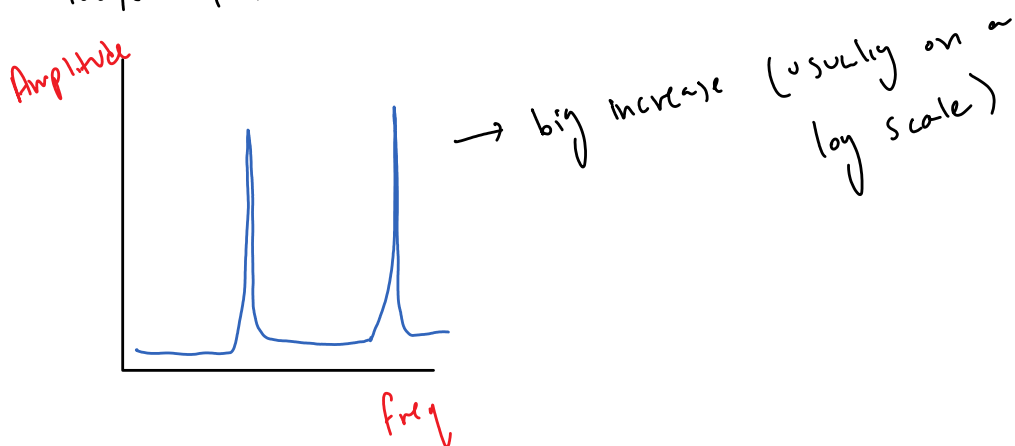
Wednesday, October 6, 2021 2:23 PM

Resonance - different objects make different sounds

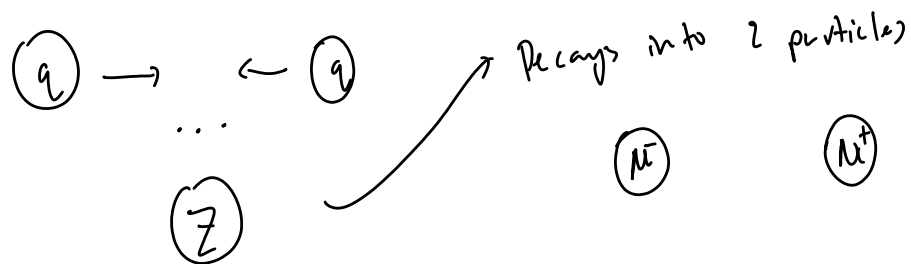
- waves at a specific frequency reinforces itself, enabling it to resonate

- related to speed of sound and object length

Way to look at resonance



Particle Physics Resonance



$$E_{\text{total}} = E_Z \rightarrow \text{in } Z \text{ r.f. (cm)}, E_Z = 91.2$$

Quantum Mechanics enables the energies to be uncertain

$$\text{So } M_Z \text{ on average} = 91.2^2$$

but $E^2 - p^2 \neq 91.2^2$

Particles that are offshell are possible, but much lower

but $E - \Gamma \neq 0$
 offshell

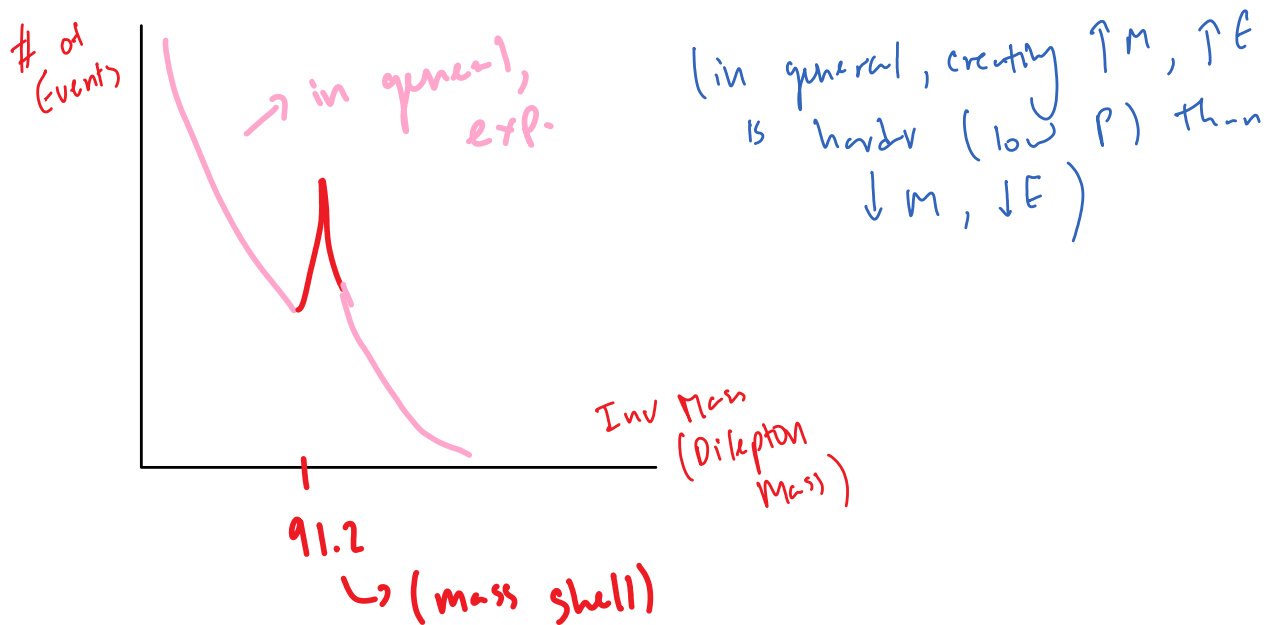
Particles that ...
 are possible, but much lower
 probabilities

Onshell \Rightarrow higher probability

→ in general, we only 'see' the muons,
 since Z decays so quickly

↳ we want to calc the invariant mass,
 since $E_{\text{cm}} = E_Z + E_{\text{Lab total, muons}}$

then $\therefore (E_{\mu_1} + E_{\mu_2})^2 - (p_{\mu_1} + p_{\mu_2})^2 = M^2$

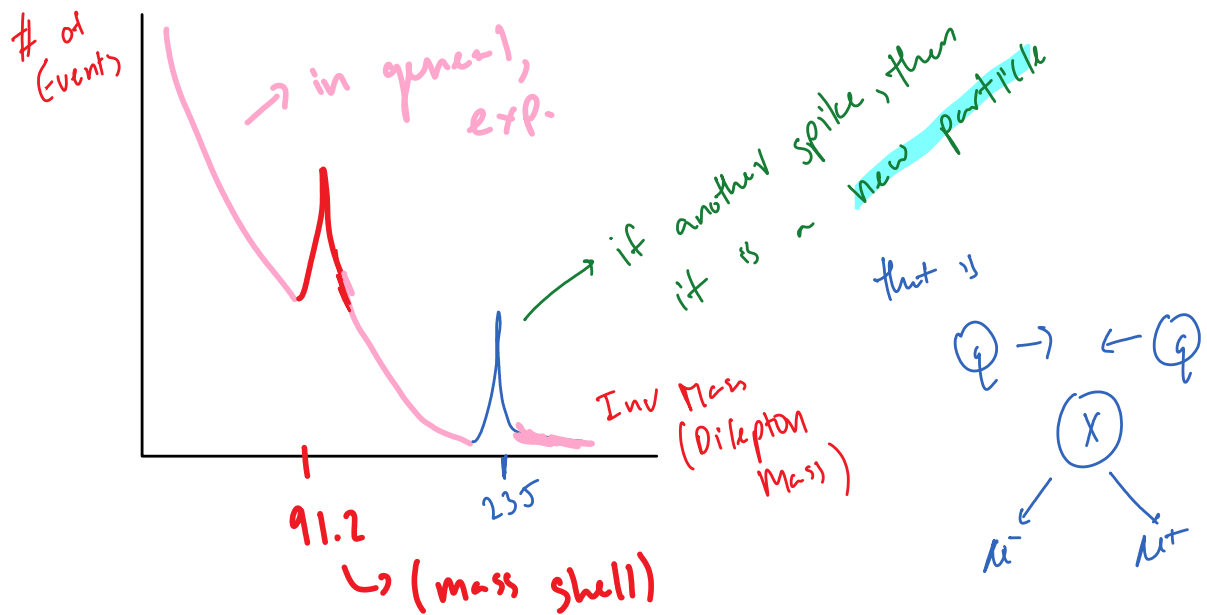


Mathematically similar to resonance graph

factor of $\frac{1}{M - M_0 + i\epsilon}$ } impedance

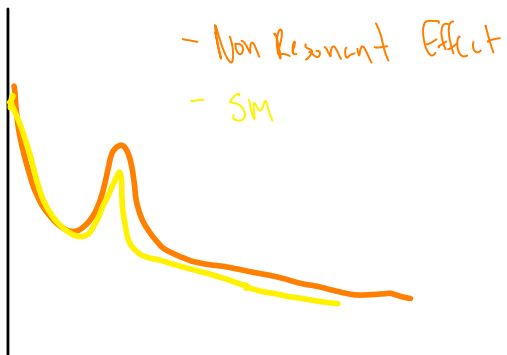
- the effect called resonance

Suppose



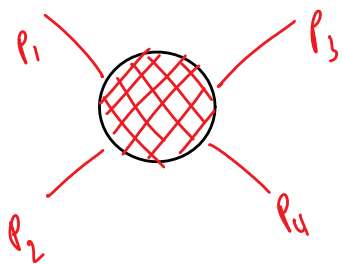
- referred to as the 'bump search'

Another method



What is \sqrt{S}

Wednesday, October 6, 2021 2:51 PM



3 invariant Quantities

$$\underbrace{(p_1 + p_2)^2}_{\text{S}}, \underbrace{(p_1 - p_3)^2}_{\text{F}}, \underbrace{(p_1 - p_4)^2}_{\text{U}}$$

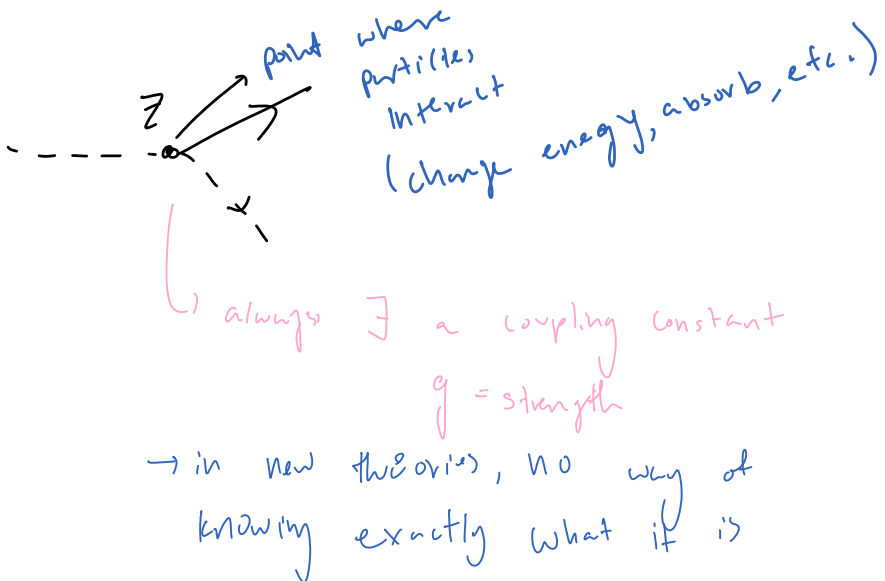
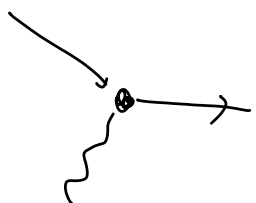
in particular,

$\sqrt{S} = p_1 + p_2$ = inv Mass of the entire system

usually = E_{cm} (currently 13 TeV) = amount of E to be turned into a mass
→ currently 13 TeV

Particle Couplings

Wednesday, October 6, 2021 2:58 PM



Lagrangian

Wednesday, October 6, 2021 3:13 PM

$$\mathcal{L} = KE - PE \quad \text{in a given system (closed)}$$

$$\text{Action } S = \int_{t_1}^{t_2} \mathcal{L} dt$$

\vec{x}_1, \bullet

- Principle of Extreme Action

the path that a particle takes
is one that extremizes (usually min)
the action

\vec{x}_2, t_2

that is, you can solve extremely
complicated systems in a scalar function

that is, start with Lagrangian \rightarrow extremize \rightarrow equations of motion

- Newtonian Approaches can get very complicated, and putting in terms of E is much simpler

- Classical Mech \rightarrow Lagrangian

\Rightarrow Euler-Lagrange equations

$$\frac{\partial \mathcal{L}}{\partial x} = \frac{d}{dt} \left(\frac{\partial \mathcal{L}}{\partial \dot{x}} \right) = 0 \quad \text{to extremize}$$

Feynman found a way to use Lagrangian to Q.M.

\mathcal{L} works in General Relativity and Q.M.



Fusion = Quantum field theory

Feynman Path Integral \Rightarrow the path a particle takes is the sum of all possible paths

$$\text{Matrix element} = M = \int e^{i\lambda \underbrace{\int_{-\infty}^{\infty} \int_{-\infty}^{\infty} \int_{-\infty}^{\infty} \int_{-\infty}^{\infty}}_{\text{4D integral over time / space}} \mathcal{L}(\phi)} d\phi$$

Non interacting Lagrangian $\mathcal{L} = [c E - m \dot{x}]$

$$\mathcal{L}(f(x)) = \mathcal{L}(x) \rightarrow \text{Lagrangian Symmetry}$$

$U(1)$ = unitary 1×1 matrix
↳ rather 1 function ex. $e^{i\theta}$

① \mathcal{L} obeys global $U(1)$ symmetry

② Regular \mathcal{L} obeys local $U(1)$ symmetry

③ It doesn't, so add terms but no

Klein-Gordon Equation \Rightarrow $\square^2 p^\mu = m^2$

quantize to obtain g-m eqn $E^2 - p^2 = m^2$

Photon: represented by a vector $\begin{pmatrix} E \\ \vec{p} \end{pmatrix}$

components related to spin states
not independent of each other

Ex: $\begin{pmatrix} a \\ b \end{pmatrix}$ s.t. $a+b=15$

let $a=7$ (gauge) \rightarrow choose a gauge that locks down one variable

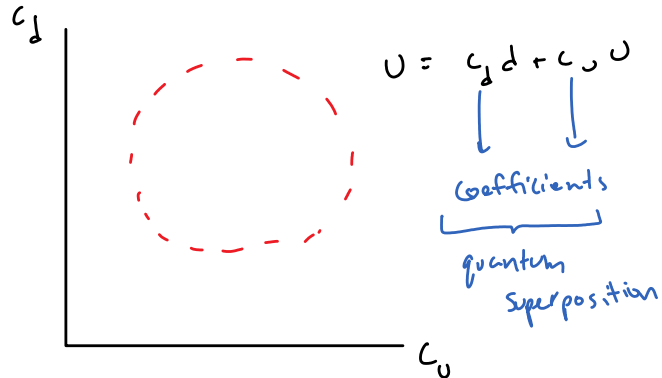
(other than massless bosons - locks down 2)

Particles you apply this choice of gauge boson are called gauge bosons.
'γ like'

Mixing

Wednesday, October 13, 2021 2:30 PM

$$\textcircled{b} \quad \left\{ \begin{array}{l} 99.9\% b \\ 0.05\% s \\ 0.05\% d \end{array} \right. \Rightarrow \text{particles that we measure are not necessarily 100\% of that flavor}$$



Vectors in physics \rightarrow something that obeys certain rules

$$\vec{v} \quad P(\vec{v}) = -\vec{v} \Rightarrow \vec{v}$$

(parity operator)

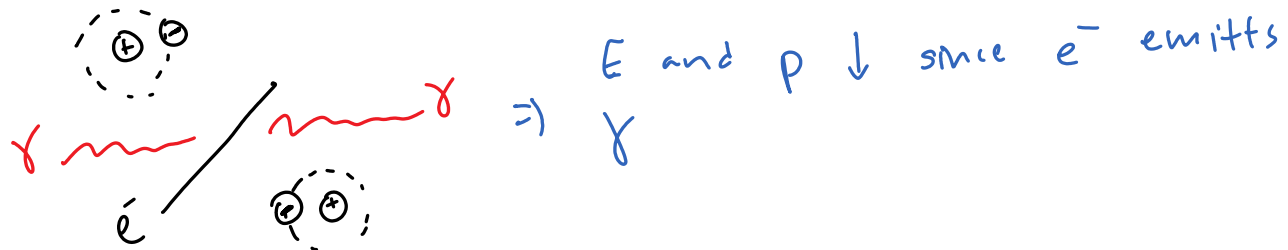
\hookrightarrow this is what makes it a vector

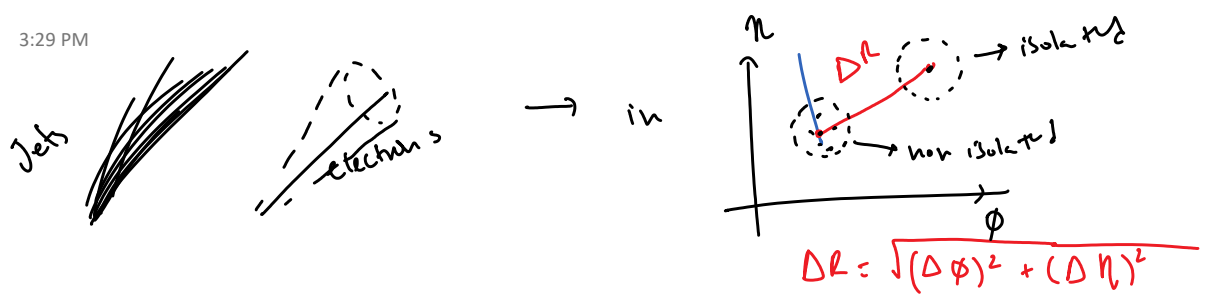
Cross product of 2 vectors in physics does not give another vector

$$\Rightarrow P(\vec{C}) = P(\vec{A} \times \vec{B}) = -\vec{A} \times \vec{B} = \underbrace{\vec{A} \times \vec{B}}_{\text{axial vectors}} = \vec{C}$$

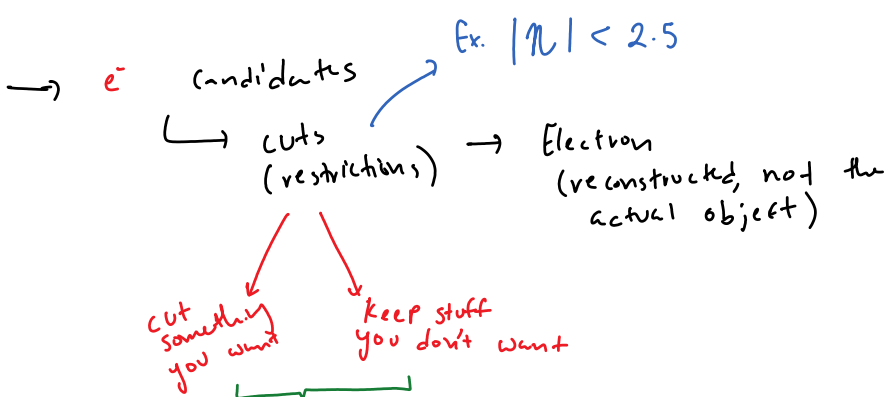
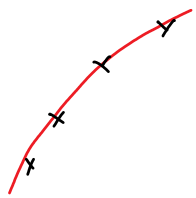
because $P(\vec{C}) = \vec{C} \Rightarrow$ cross product is not a vector
(pseudovectors)

Bremsstrahlung = braking radiation





Lepton Reconstruction



- calculate how often we keep the real electron (efficiency)

- how often we keep fake electrons (fake rates)

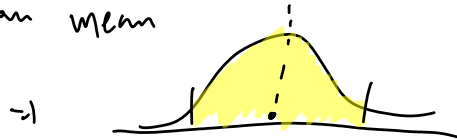
Stat uncertainty \sqrt{N}

by $1/\sqrt{N} \rightarrow$ sample size

} Particle physics is
Very conservative

Quadrature sum:
totl: $\sqrt{-3^2 + 1.1^2 + .05^2}$

We assume that each of the uncertainties are 1 std. dev away from mean



Buschmann

Wednesday, October 27, 2021 1:46 PM

Lepton Jets from Radiating Dark Matter

Malte Buschmann,^{1,*} Joachim Kopp,^{1,†} Jia Liu,^{1,‡} and Pedro A.N. Machado^{2,§}

¹PRISMA Cluster of Excellence and Mainz Institute for Theoretical Physics,
Johannes Gutenberg University, 55099 Mainz, Germany

² Departamento de Física Teórica and Instituto de Física Teórica, IFT-UAM/CSIC,
Universidad Autónoma de Madrid, Cantoblanco, 28049, Madrid, Spain

(Dated: July 14, 2015)

The idea that dark matter forms part of a larger dark sector is very intriguing, given the high degree of complexity of the visible sector. In this paper, we discuss lepton jets as a promising signature of an extended dark sector. As a simple toy model, we consider an $\mathcal{O}(\text{GeV})$ DM fermion coupled to a new $U(1)'$ gauge boson (dark photon) with a mass of order GeV and kinetically mixed with the Standard Model photon. Dark matter production at the LHC in this model is typically accompanied by collinear radiation of dark photons whose decay products can form lepton jets. We analyze the dynamics of collinear dark photon emission both analytically and numerically. In particular, we derive the dark photon energy spectrum using recursive analytic expressions, using Monte Carlo simulations in Pythia, and using an inverse Mellin transform to obtain the spectrum from its moments. In the second part of the paper, we simulate the expected lepton jet signatures from radiating dark matter at the LHC, carefully taking into account the various dark photon decay modes and allowing for both prompt and displaced decays. Using these simulations, we recast two existing ATLAS lepton jet searches to significantly restrict the parameter space of extended dark sector models, and we compute the expected sensitivity of future LHC searches.

I. INTRODUCTION

For decades, nature has been keeping us completely in the dark about the nature of dark matter. In view of this, the scope of theoretical and phenomenological studies has become significantly broader than it used to be some years ago. An often discussed possibility nowadays is a dark sector featuring new gauge interactions. Phenomenologically, such new gauge interactions can for instance lead to Sommerfeld enhancement of the **dark matter (DM) annihilation cross section** [1–3], to DM self-interactions [4, 5], which may affect small scale structures in the Universe such as dwarf galaxies, or to DM bound states [6–8]. In this context, it is worth noting that there are long-standing discrepancies between theory and small scale structure observations, which could be explained either by dark matter **self interactions** [4, 5] or by **baryonic feedback** [9, 10]. Also recent observations of the galaxy cluster Abell 3827 could point towards self-interacting DM [11] (see, however, [12]).

Here, we discuss the prospects of detecting new gauge interactions in the dark sector at the LHC. We work in a simplified model with a dark matter fermion χ and a $U(1)'$ gauge boson A' (dark photon), kinetically mixed with the photon [3, 13] (see e.g. [14] for a review). This model, which we dub *radiating dark matter*, serves here as a proxy for a large class of more complicated scenarios, to which our conclusions can be applied as well. If the dark matter and dark photon masses are relatively small compared to the *typical partonic center of mass energy* at the LHC, emission of dark photons from a dark matter particle receives a strong enhancement in the collinear direction. This is analogous to the emission of collinear photons in QED or the emergence of a

*Electronic address: buschmann@uni-mainz.de

[†] Electronic address: jkopp@uni-mainz.de

[†] Electronic address: liuj@uni-mainz.de

[§]Electronic address: pedro.machado@uam.es

↗ radiation?

parton shower in QCD. Thanks to the collinear enhancement, DM production at the LHC is typically accompanied by the emission of several dark photons whose subsequent decay leads to a collimated jet of SM particles. These SM particles will often include electrons or muons, resulting in a *lepton jet* signature. Depending on the dark photon decay length, the SM particles in the lepton jets can be produced close to the primary interaction vertex (prompt lepton jets) or further away from it (displaced lepton jets). In this paper, we explore both prompt and displaced lepton jets from the theoretical and from the phenomenological side. In particular, we derive semi-analytic expressions for the spectrum of radiated A' particles, and we compute limits on $U(1)'$ models from two ATLAS lepton jet searches [15, 16]. We also discuss how the discovery potential will improve the 13 TeV LHC.

Lepton jets have been discussed previously in various contexts. In supersymmetric models, they can be a signal of cascade decays of heavy new particles into much lighter states which subsequently decay to lepton pairs [17–22]. Lepton jets could also arise in models featuring non-standard Higgs decays to dark sector particles that subsequently decay to leptons [23–26]. DM production in association with a single radiated A' boson have been discussed in [26, 27]. If the A' is heavy, it can be reconstructed as a dilepton resonance, while for light A' , a narrow hadronic jet from its decay to quarks can be a promising signature, especially since an A' -induced jet could be distinguished from a QCD jet by using jet substructure techniques [28]. In related works, multi-lepton final states at B factories have been studied in [29, 30]. Several recent papers discuss how strong dynamics in the dark sector can lead to the formation of a dark parton shower, with subsequent decay of dark sector particles into hadronic jets with non-standard properties like displaced vertices, high multiplicities of vertices in the jet cone [31] and significant missing energy aligned with a jet [32]. It is even possible that the DM itself interacts relatively strongly with SM particles, so that its production at a collider would lead to jets rather than the usual missing energy signature [33]. An experimental search for displaced hadronic jets has been presented in [34] by the ATLAS collaboration.

The plan of this paper is as follows: in sec. II, we introduce our simplified model of radiating dark matter and discuss its main phenomenological features. We then analyze the physics of dark photon showers in sec. III both analytically and numerically. We derive the expected spectrum of radiated dark photons in three different ways: using recursive integral expressions, using an inverse Mellin transform to compute the spectrum from its moments, and using a Monte Carlo simulation in Pythia 8.2 [35–37]. Our main phenomenological results are presented in sec. IV. There, we recast the existing ATLAS searches for prompt lepton jets [15] and for displaced lepton jets [16] to set limits on our dark radiation model, and we also compute the sensitivity of future LHC searches at 13 TeV center of mass energy. We summarize our results and conclude in sec. V.

II. MODEL

A. The Lagrangian

The results of this paper can be applied to any model in which a $\lesssim 10$ GeV DM particle interacts with a new $\lesssim 10$ GeV gauge boson, as long as the typical energy at which DM particles are produced at the LHC is much higher than their masses. To illustrate our main points, we will use a specific toy model of radiating DM, in which the dark sector consists of a fermionic DM particle χ and a massive $U(1)'$ gauge boson A' . The coupling strength between χ and A' is described by a dark fine structure constant $\alpha_{A'} \equiv g_{A'}^2/(4\pi)$. Moreover, the dark photon A' is kinetically mixed with the SM photon. The Lagrangian for the dark sector is thus

$$\mathcal{L}_{\text{dark}} \equiv \bar{\chi}(i\cancel{D} - m_\chi + ig_{A'}\cancel{A}')\chi - \frac{1}{4}F'_{\mu\nu}F'^{\mu\nu} - \frac{1}{2}m_{A'}^2 A'_\mu A'^\nu - \frac{\epsilon}{2}F'_{\mu\nu}F^{\mu\nu}, \quad (1)$$

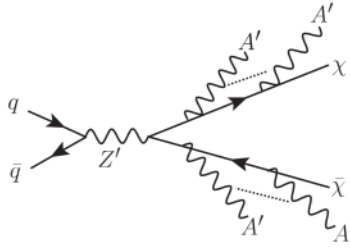


FIG. 1: Feynman diagram for dark matter pair production at the LHC through an s -channel Z' resonance, followed by “dark radiation”, i.e. emission of several—mostly soft or collinear—dark photons.

where $m_{A'}$ and m_χ are the masses of A' and χ , respectively. We denote by $F^{\mu\nu}$ and $F'^{\mu\nu}$ the field strength tensors of the SM photon and the dark photon A' , respectively. The dimensionless coupling constant ϵ describes the strength of the kinetic mixing between the A' and the photon. Due to $SU(2)$ invariance, the A' should also mix kinetically with the Z , but effects of this mixing are suppressed by factors of $m_{A'}^2/M_Z^2$ and are therefore neglected in the following.

Since the kinetic mixing between A' and the photon is too small to lead to significant DM production at the LHC, we assume an additional DM–SM coupling. For definiteness, we take this coupling to be through a heavy s -channel vector resonance Z' with couplings to all quark flavors and to dark matter. Since the dynamics of dark radiation does not depend on the primary DM production mechanism but only on the production cross section and to some extent on the DM energy spectrum, our results will apply to any model in which DM particles can be produced in significant numbers at the LHC, including for instance models with contact interactions, t -channel mediators, or Higgs portal interactions. The relevant terms in the Lagrangian of our toy model are

$$\mathcal{L}_{Z'} \equiv g_q \sum_f \bar{q}_f Z' q_f + g_\chi \bar{\chi} Z' \chi, \quad (2)$$

where q_f is the SM quark field of flavor f and g_q, g_χ are the Z' couplings to quarks and DM particles, respectively. For simplicity, we have assumed the coupling to quarks to be flavor universal.

Fig. 1 illustrates DM pair production at the LHC via s -channel Z' exchange, followed by radiation of several dark photons. Due to the assumed lightness of χ and A' , the emission is enhanced in the collinear direction. Due to this enhancement, with a moderate dark fine structure constant $\alpha_{A'} \sim \mathcal{O}(0.1)$, we typically expect a few dark photons to be radiated in each DM pair production process. We will discuss the dynamics of this “dark radiation” in sec. III using a formalism analogous to parton showers in QCD.

B. Benchmark points

We define two benchmark points in the parameter space of our toy model, which we will use to illustrate our main points in secs. III and IV. In sec. IV, we will also discuss in detail how departing from these benchmark points affects our results. The two benchmark points A and B are summarized in table I, together with several phenomenological observables derived from them.

In both cases, we assume a Z' mass of 1 TeV. We choose g_q and g_χ such that the resonant Z' production cross section is about 1 pb at the 8 TeV LHC for benchmark point A, and about a factor of 10 smaller for benchmark point B. In both cases, the Z' has a branching ratio $\sim 85\%$ for the decay $Z' \rightarrow \bar{\chi}\chi$. We choose both m_χ and $m_{A'}$ to be of order GeV or below. Together with a moderately large dark fine structure constant $\alpha_{A'} = 0.2$, this leads to the radiation of a significant number of A' bosons when DM is produced at the LHC. Note that the number of

	$m_{Z'}$ [TeV]	g_q	g_χ	m_χ [GeV]	$m_{A'}$ [GeV]	$\alpha_{A'}$	$c\tau$ [mm]	ϵ	$\sigma_7(Z')$ [10^{-6}]	$\sigma_8(Z')$ [pb]	$\sigma_{13}(Z')$ [pb]	$\Gamma_{Z'}$ [pb]	$\text{BR}(Z' \rightarrow \chi\bar{\chi})$	$2\langle n_{A'} \rangle_8$	$2\langle n_{A'} \rangle_{13}$
A	1	0.1	1	4	1.5	0.2	10	2.8	0.58	0.85	2.7	31.3	84.8%	3.50	3.51
B	1	0.03	0.3	0.4	0.4	0.2	1	24	0.052	0.076	0.244	2.82	84.8%	5.15	5.17

TABLE I: Values of the model parameters $m_{Z'}$ (heavy mediator mass), g_q , g_χ (heavy mediator couplings), m_χ (DM mass), $m_{A'}$ (dark photon mass), $\alpha_{A'}$ (dark fine structure constant) and $c\tau$ (dark photon decay length) at our two benchmark points A and B. We also show the resulting values for several derived quantities, in particular the kinetic mixing ϵ corresponding to the given $c\tau$ and $m_{A'}$, the resonance cross sections $\sigma_7(Z')$, $\sigma_8(Z')$ and $\sigma_{13}(Z')$ for Z' production $pp \rightarrow Z'$ at the 7 TeV, 8 TeV and 13 TeV LHC, respectively, the total decay width $\Gamma_{Z'}$ of the heavy mediator, its branching ratio to DM pairs, and the average numbers $2\langle n_{A'} \rangle_8$ ($2\langle n_{A'} \rangle_{13}$) of radiated dark photons in each DM pair production event at the 8 TeV (13 TeV) LHC.

radiated A' bosons is almost independent of the collider center of mass energy because the boost of the primary DM particles, which determines the amount of radiation, is mostly dictated by the s -channel Z' resonance. We choose the dark photon decay length $c\tau$ such that at benchmark point A, most dark photons will decay far from their production vertex, while at benchmark point B, the displacement of the decay vertex is much smaller. Thus, benchmark point A is in the realm of lepton jet searches requiring displaced decay vertices, while benchmark point B is most easily detectable in searches for prompt lepton jets. Note that in table I we treat $c\tau$ as a fundamental parameter and ϵ as a derived quantity. This will only be relevant when we vary the model parameters around their benchmark values in sec. IV (figs. 6 and 7). To make the discussion there more transparent, we choose to keep $c\tau$ rather than ϵ fixed when varying the other model parameters. Of course, as long as all other model parameters are fixed, there is a one-to-one correspondence between $c\tau$ and ϵ .

Our parameter choices are consistent with existing collider constraints: In particular, dijet searches do not exclude Z' bosons with the parameters chosen here [38, 39]. For instance, the ATLAS dijet search in 20.3 fb^{-1} of 8 TeV LHC data [38] restricts the product $\sigma(Z') \times \text{BR}(Z' \rightarrow qq) \times A$ of the Z' production cross section, the branching ratio to a quark–antiquark final state, and the experimental acceptance factor $A \sim 0.6$ to be $\lesssim 1 \text{ pb}$ at 95% confidence level (CL). The corresponding CMS search [39] does not explicitly quote a limit at $m_{Z'} = 1 \text{ TeV}$, but noting that no spectral feature is observed at this mass, the limits given on heavier Z' bosons can be extrapolated down, indicating that the CMS limit is stronger than the ATLAS limits by perhaps a factor of two. The acceptance factor is similar in ATLAS and CMS. Limits on dijet resonances are also provided by the CDF experiment at the Tevatron, yielding $\sigma(Z') \times \text{BR}(Z' \rightarrow qq) \times A \lesssim 0.11 \text{ pb}$ [40]. Since CDF requires both jets to have a rapidity $|y| < 1$, we conservatively estimate the acceptance in CDF is not larger than in CMS. Including an acceptance factor of 0.6, we predict at our benchmark point A $\sigma(Z') \times \text{BR}(Z' \rightarrow qq) \times A = 0.08 \text{ pb}$ at the 8 TeV LHC and $\sigma(Z') \times \text{BR}(Z' \rightarrow qq) \times A = 0.001 \text{ pb}$ at the Tevatron, which is clearly consistent with the above constraints. The $pp \rightarrow Z' \rightarrow \chi\bar{\chi}$ production cross sections at benchmark point B are even smaller.

DM production through heavy resonances is also constrained by monojet searches [41, 42]. ATLAS sets a lower limit $m_{Z'}/\sqrt{g_q g_\chi} \gtrsim 2 \text{ TeV}$ [41], whereas we have $m_{Z'}/\sqrt{g_q g_\chi} \sim 3.2 \text{ TeV}$ at benchmark point A and $m_{Z'}/\sqrt{g_q g_\chi} \sim 10 \text{ TeV}$ at benchmark point B. Both benchmark points thus satisfy the limit.

We also need to consider cosmological constraints on the dark sector of our toy model. The most important question here is whether χ can be a thermal relic and account for all of the DM in the Universe. If there is no particle–antiparticle asymmetry in the dark sector, the answer is no.

The reason is that at our benchmark points the annihilation cross section [43]

$$\langle\sigma v\rangle_{\bar{\chi}\chi \rightarrow A'A'} \simeq \frac{\pi\alpha_{A'}^2}{m_\chi^2} \frac{(1-m_{A'}^2/m_\chi^2)^{3/2}}{(1-\frac{1}{2}m_{A'}^2/m_\chi^2)^2} \quad (3)$$

is much larger than the thermal relic cross section of few $\times 10^{-26}$ cm³/sec. Reducing the annihilation cross section would either require a significantly smaller $\alpha_{A'}$, precluding significant dark radiation at the LHC, or a larger A' mass, in particular $m_{A'} > m_\chi$. In the latter case, only the annihilation channel $\bar{\chi}\chi \rightarrow \bar{q}q$ would remain open. The cross section for this channel is [44, 45]

$$\langle\sigma v\rangle_{\bar{\chi}\chi \rightarrow \bar{q}q} \simeq \frac{3N_f g_q^2 g_\chi^2}{2\pi} \frac{2m_\chi^2 + m_q^2}{(4m_\chi^2 - m_{Z'}^2)^2} \sqrt{1 - \frac{m_q^2}{m_\chi^2}}, \quad (4)$$

where N_f is the number of kinematically accessible quark flavors. Since $\langle\sigma v\rangle_{\bar{\chi}\chi \rightarrow \bar{q}q}$ scales as $g_q^2 g_\chi^2 m_\chi^2 / m_{Z'}^4$, it is much smaller than the thermal relic value for the small χ masses that we are interested in here. It would thus lead to overclosure of the Universe. For symmetric DM models, we therefore conclude that χ must be a subdominant component of the DM in the Universe¹. This, of course, does not change the LHC phenomenology that we are interested in here, it only means that our toy model cannot provide a complete description of the dark sector. The fact that for symmetric DM models a discovery of χ through a dark radiation signature is only possible if χ is a subdominant component of DM is in line with the general statement that, in models with multiple thermally produced DM components, it is likely that the subdominant DM components are discovered at the LHC first due to their larger interaction strengths. For asymmetric DM, i.e. DM with a primordial particle–antiparticle asymmetry generated at some high scale, χ could account for all of the DM in the Universe. In this case, the large annihilation cross section to A' pairs is not a problem but a feature because it allows for efficient annihilation of the symmetric component of the primordial DM soup. However another opposite charge particle might be needed due to gauge invariance for such light A' [47]. Let us emphasize that, in this paper, we will indiscriminately call χ the dark matter, even though the above discussion shows that it does not need to be the dominant DM component.

Next, let us comment on constraints from direct and indirect DM searches. Without a primordial χ – $\bar{\chi}$ asymmetry, both types of constraints are easily satisfied due to the required small relic abundance of χ . For asymmetric DM, indirect searches are also insensitive because $\chi\bar{\chi}$ annihilation is impossible in such models. The sensitivity of direct detection experiments is limited due to the small m_χ at our benchmark points. For benchmark point B with $m_\chi = 0.4$ GeV, the DM mass is obviously below the direct detection threshold, while for benchmark point A with $m_\chi = 4$ GeV, one might worry about limits from low-threshold experiments. The best limit in this mass range comes from CDMSlite and requires the spin-independent χ –nucleon scattering cross section $\sigma_{\chi N}$ to be below 1.5×10^{-40} cm² if χ accounts for all of the DM in the Universe [48]. Our prediction at benchmark point A is $\sigma_{\chi N} \simeq 6.5 \times 10^{-42}$ cm², avoiding the bound by more than an order of magnitude.

A different set of bounds on our model comes from the fact that χ particles have self-interactions, mediated by the A' boson. Such DM self-interactions are constrained by observations of colliding galaxy cluster (most notably the Bullet Cluster) [49] and by measurements of the ellipticity of DM halos of groups of galaxies [50]. The resulting limit on the DM self-scattering cross-section is

$$\sigma_{\chi\chi}/m_\chi \lesssim 1 \text{ cm}^2/\text{g} = 1.78 \times 10^{-24} \text{ cm}^2/\text{GeV}. \quad (5)$$

¹ There is an exception when A' mass is slightly higher than χ mass, one can exponentially reduce the thermal averaged annihilation cross section and achieve the right relic abundance [46].

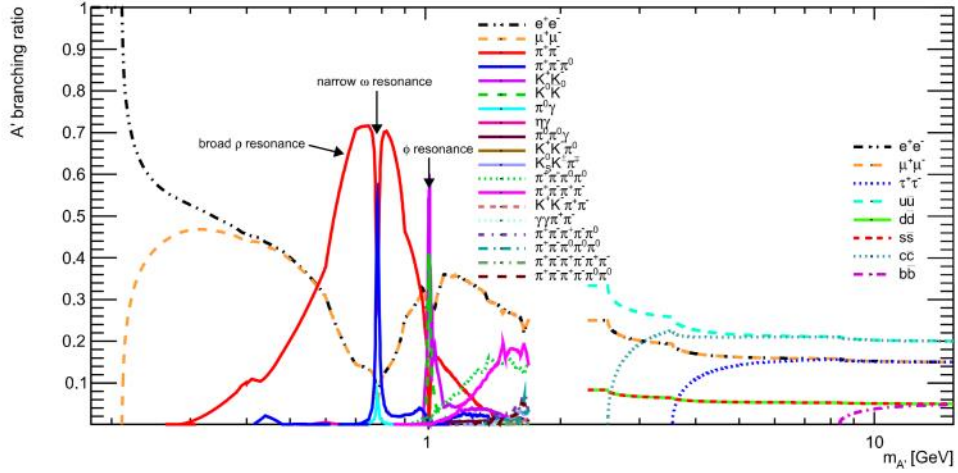


FIG. 2: Branching ratios for the 19 dark photon decay channels included in our analysis as a function of the dark photon mass.

Obviously, this constraint applies only if χ forms the bulk of the DM in the Universe. As explained above, this is only possible in our scenario if there is a particle–antiparticle asymmetry in the dark sector. In the perturbative regime, where $\alpha_{A'} m_\chi / m_{A'} \lesssim 1$, a simple calculation shows that the predicted non-relativistic self-scattering cross section is [5]

$$\sigma_{\chi\chi}/m_\chi \simeq 5 \times 10^{-31} \text{ cm}^2/\text{GeV} \times \left(\frac{\alpha_{A'}}{0.1}\right)^2 \left(\frac{m_\chi}{\text{GeV}}\right) \left(\frac{\text{GeV}}{m_{A'}}\right)^4. \quad (6)$$

For our benchmark point A (B) from table I, this leads to $\sigma_{\chi\chi}/m_\chi \simeq 10^{-30} \text{ cm}^2/\text{GeV}$ ($10^{-29} \text{ cm}^2/\text{GeV}$), well within the observational limit.

Regarding the dark photon mass $m_{A'}$ and its kinetic mixing ϵ with the SM photon, strong constraints exist from low energy experiments and from astrophysics. These constraints require $\epsilon \lesssim 10^{-10}$ for $m_{A'} \lesssim 10 \text{ MeV}$, but relax to $\epsilon \lesssim 10^{-3}$ for $10 \text{ MeV} \lesssim m_{A'} \lesssim 10 \text{ GeV}$, the mass range that we are interested in here. Our benchmark points from table I are thus consistent with limits from dark photon searches. We will discuss these limits in more detail in sec. IV, see in particular fig. 8.

C. Dark Photon decay

After dark photons have been radiated from pair-produced χ particles at the LHC, they decay to SM particles via their kinetic mixing with the photon (see eq. (1)). For $m_{A'} \lesssim 2 \text{ GeV}$ and $m_{A'} < 2m_\chi$, the dominant decay modes include $A' \rightarrow e^+e^-$, $\mu^+\mu^-$, as well as decays to various hadronic resonances. The partial decay width to leptons of a specific flavor ℓ is

$$\Gamma(A' \rightarrow \ell^+ \ell^-) = \frac{1}{3} \alpha \epsilon^2 m_{A'} \sqrt{1 - 4 \frac{m_\ell^2}{m_{A'}^2}} \left(1 + 2 \frac{m_\ell^2}{m_{A'}^2}\right). \quad (7)$$

The **hadronic decay width** can be calculated using measurements of hadron production cross sections at e^+e^- colliders, in particular the ratio $R(s) \equiv \sigma(e^+e^- \rightarrow \text{hadrons})/\sigma(e^+e^- \rightarrow \mu^+\mu^-)$, where s is the center-of-mass energy. At $s = m_{A'}^2$, the ratio between the partial A' decay width

into a given hadronic final state and the partial decay width to the $\mu^+\mu^-$ final state should be equal to $R(s)$:

$$\Gamma(A' \rightarrow \text{hadrons}) = \Gamma(A' \rightarrow \mu^+\mu^-) R(s = m_{A'}^2). \quad (8)$$

We use hadronic cross-sections from refs. [51, 52] to calculate the A' decay branching ratios. We include 19 decay channels, shown in fig. 2. In the calculation, care must be taken to avoid double counting of hadronic degrees of freedom. For example, the decay $A' \rightarrow \pi^+\pi^-\pi^0\pi^0$ receives contributions both from the direct production of pions and from the decay $A' \rightarrow \omega\pi^0$, followed by $\omega \rightarrow \pi^+\pi^-\pi^0$. We choose to preferentially include channels with pions and kaons. For heavier mesons, we only include decay channels in which there is no double counting. In principle, there is also a double counting problem between kaon and pion final states because of the fully hadronic kaon decay channels. Fortunately, these channels have very small branching ratios and can be neglected.

For $m_{A'} \gtrsim 2$ GeV, hadronic A' decays are more conveniently described in QCD language as decays to quark pairs. The partial decay width to a quark pair of a given flavor q_f is

$$\Gamma(A' \rightarrow q_f \bar{q}_f) = N_c Q_{q_f}^2 \Gamma(A' \rightarrow \ell^+ \ell^-)|_{m_\ell = m_{q_f}}, \quad (9)$$

where Q_{q_f} is the electric charge of q_f and $N_c = 3$ is a color factor. At intermediate A' masses ~ 2 GeV, a very large number of hadronic resonances appears, so that neither the QCD description in terms of quark final states nor the low energy effective theory involving just a few hadronic states are applicable. We therefore do not consider this mass range in the following, but we will see in sec. IV that our results on the LHC sensitivity can be smoothly interpolated between the QCD regime and the low-energy regime.

III. DARK PARTON SHOWER

Before presenting our numerical results, let us provide some analytic discussion of dark photon radiation. Part of the following discussion is based on refs. [53, 54]. We first note that factorization theorems ensure that the cross section can be factorized into short range (hard process) and long range (shower) contributions [55]. Thus, we can treat the dark photon shower as independent of the primary $\bar{\chi}\chi$ production process. The relevant processes in the development of an A' shower are $\chi \rightarrow \chi + A'$ and $A' \rightarrow \bar{\chi}\chi$. In the following, we include only the first process, which is shown also in fig. 3. Its probability is much larger than the probability for $A' \rightarrow \bar{\chi}\chi$ due to the structure of the respective splitting kernels. In particular, the splitting kernel for $A' \rightarrow \bar{\chi}\chi$ is not divergent in the soft limit, in analogy to photon splitting in QED. The radiation of gauge bosons from fermions, on the other hand, is formally divergent in the soft and collinear phase space regions. In our scenario, the dark matter and dark photon masses regularize the radiation probability in these regions by providing a natural infrared cut-off. From a phenomenological point of view, we are more interested in collinear emission than in soft emission because the decay products of very soft dark photons would not be detectable at the LHC. We work under the assumption of strongly ordered emission, i.e. the virtuality of the incoming particle in a splitting process is assumed to be much larger than the virtuality of the outgoing particles. The latter are therefore treated as on-shell. Within the strongly ordered emission assumption, we can consider each splitting $\chi \rightarrow \chi + A'$ as an isolated process, since a secondary splitting would be a small perturbation with respect to the first one.

The differential probability for a collinear splitting can be written as

$$\frac{\alpha_{A'}}{2\pi} dx \frac{dt}{t} P_{\chi \rightarrow \chi}(x, t), \quad (10)$$

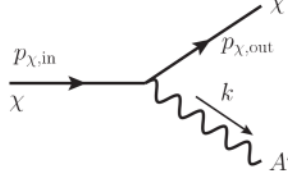


FIG. 3: Radiation of a single dark photon A' from a DM particle χ .

where t is the virtuality of the incoming DM particle and x is the fraction of its energy that is transferred to the outgoing DM particle. The quantity $P_{\chi \rightarrow \chi}(x, t)$ is the splitting kernel that encodes the model-dependent details of the splitting probability. We call attention to the fact that we treat $\alpha_{A'}$ as independent of t , i.e. we neglect renormalization group running. Since the running is logarithmic, it will not play a major role in the development of the dark photon shower. Moreover, the running would depend on the full particle content of the dark sector and is thus highly model dependent. Eq. (10) can be understood as the squared matrix element of the splitting process, multiplied by the propagator of the incoming DM particle and integrated over the phase space of the outgoing particles. In the limit $t \rightarrow 0$ (highly collinear splitting), the propagator factor $1/t$ in eq. (10) diverges as expected. It is prevented from going all the way to zero thanks to the non-zero dark photon mass.

A. Kinematics and notation

We write the off-shell 4-momentum of the incoming DM particle in a given splitting process as (see ref. [54] for a slightly different approach)

$$p_{\chi,\text{in}} = (E, 0, 0, p). \quad (11)$$

Notice that in general $E \neq \sqrt{\hat{s}}/2$. For instance, if the second χ particle, which we call the spectator, is on-shell and does not radiate, energy momentum conservation requires its three-momentum to be $(0, 0, -p)$. This fixes the energy of the spectator to be $E_s^2 = p^2 + m_\chi^2$, and hence $E \geq E_s + m_{A'}$ if at least one dark photon is radiated in the event. In the following, we will nevertheless assume $E = E_s = \sqrt{\hat{s}}/2$, the so called collinear approximation. Naturally, we expect it to fail when $m_{A'} + m_\chi \sim E$, or when the opening angle between the splitting products is large, so the splitting is not collinear any more.

The on-shell 4-momenta of the outgoing DM particle and dark photon after the splitting are

$$p_{\chi,\text{out}} = (xE, -k_t, 0, \sqrt{x^2 E^2 - k_t^2 - m_\chi^2}), \quad (12)$$

and

$$k = ((1-x)E, k_t, 0, \sqrt{(1-x)^2 E^2 - k_t^2 - m_{A'}^2}), \quad (13)$$

respectively. Since the energies of the outgoing particles must be larger than their masses and because energies and momenta have to be positive, the following constraints must be fulfilled:

$$m_\chi/E < x < 1 - m_{A'}/E, \quad x^2 E^2 - m_\chi^2 \geq k_t^2, \quad (1-x)^2 E^2 - m_{A'}^2 \geq k_t^2. \quad (14)$$

The first relation defines in particular the allowed range of the variable x in the splitting probability eq. (10). Unfortunately, this range depends on E and thus on all preceding splitting processes.

This would preclude us from treating the dark photon shower analytically. Therefore, we will in the following take the minimum and maximum values of x to be

$$x_{\min} \equiv m_\chi/E_0, \quad x_{\max} \equiv 1 - m_{A'}/E_0, \quad (15)$$

where E_0 is the initial energy of the DM particle χ before emission of the first dark photon. Since most emitted dark photons are soft, we expect E to be close to E_0 for most splittings. The relations (15) would even be exact for $m_\chi = m_{A'} = 0$, but since we have $m_\chi, m_{A'} \ll E_0$, we expect them to be very good approximations also in our case.

The virtuality t is defined as

$$t \equiv (p_{\chi,\text{out}} + k)^2 - m_\chi^2 = m_{A'}^2 + 2p_{\chi,\text{out}} \cdot k, \quad (16)$$

and the splitting kernel is given by [56]

$$P_{\chi \rightarrow \chi}(x, t) = \frac{1+x^2}{1-x} - \frac{2(m_\chi^2 + m_{A'}^2)}{t}. \quad (17)$$

We see that $P_{\chi \rightarrow \chi}(x, t)$ becomes large for $x \rightarrow 1$, where the emitted dark photon is very soft. Since we are dealing with massive dark photons, x is kinematically required to always be < 1 (see eqs. (14) and (15)). In the following, we will neglect the mass dependent term in $P_{\chi \rightarrow \chi}$ and call the thus approximated splitting kernel $P_{\chi \rightarrow \chi}(x)$. Like the approximation used for x_{\min} and x_{\max} above, also this approximation is necessary to make different splittings completely independent of each other, a precondition for our analytic calculations.

In order to also regularize the collinear $t \rightarrow 0$ divergence in eq. (10), care must be taken also when choosing the integration limits for t . The lower bound t_{\min} for t is obtained when $k_t \rightarrow 0$, that is

$$\begin{aligned} t_{\min}(x) &= m_{A'}^2 + 2p_{\chi,\text{out}} \cdot k|_{k_t \rightarrow 0} \\ &= m_{A'}^2 + 2\left(E^2 x(1-x) - \sqrt{x^2 E^2 - m_\chi^2} \sqrt{(1-x)^2 E^2 - m_{A'}^2}\right), \end{aligned} \quad (18)$$

while the upper bound is obtained when k_t is maximal, within the constraints (14), that is,

$$t_{\max}(x) = m_{A'}^2 + 2p_{\chi,\text{out}} \cdot k|_{k_t,\max}, \quad (19)$$

with

$$k_{t,\max}^2(x) = \min \{(1-x)^2 E^2 - m_{A'}^2, x^2 E^2 - m_\chi^2\}. \quad (20)$$

Interestingly, when x takes its maximum or minimum value allowed by eq. (14), $k_{t,\max}$ becomes 0, which leads $t_{\min} = t_{\max}$ and the splitting probability goes to 0. As in eq. (15), we will in the following take $E \rightarrow E_0$ also when evaluating t_{\min} and t_{\max} . This approximation is necessary to make consecutive splitting processes completely independent and thus treat the dark photon shower analytically.

B. Number of emitted dark photons

A DM particle is produced at the LHC with a certain maximal virtuality t_{\max} and then radiates in general several dark photons. In each splitting, its virtuality is reduced, until it finally reaches the infrared cutoff t_{\min} . The expectation value for the number of radiated dark photons is

$$\langle n_{A'} \rangle \simeq \frac{\alpha_{A'}}{2\pi} \int_{x_{\min}}^{x_{\max}} dx \int_{t_{\min}}^{t_{\max}} \frac{dt}{t} P_{\chi \rightarrow \chi}(x). \quad (21)$$

Note that this compact expression is valid only if we neglect the t -dependence of the splitting kernel and of the integration boundaries x_{\min} , x_{\max} , t_{\min} , t_{\max} defined in the previous section.

The probability that a DM particle χ radiates exactly m dark photons is given by a Poisson distribution [53]:

$$p_m = \frac{e^{-\langle n_{A'} \rangle} \langle n_{A'} \rangle^m}{m!}. \quad (22)$$

To see this, note that eq. (10) implies that the probability for *no* splitting to occur between t_{\max} and t_{\min} is given by the Sudakov factor

$$\Delta(t_{\min}, t_{\max}) \equiv e^{-\langle n_{A'} \rangle}, \quad (23)$$

with $\langle n_{A'} \rangle$ defined in eq. (21). The probability for exactly one splitting is then

$$\begin{aligned} p_1 &= \frac{\alpha_{A'}}{2\pi} \int_{x_{\min}}^{x_{\max}} dx \int_{t_{\min}}^{t_{\max}} \frac{dt}{t} \Delta(t_{\min}, t) P_{\chi \rightarrow \chi}(x) \Delta(t, t_{\max}) \\ &= e^{-\langle n_{A'} \rangle} \langle n_{A'} \rangle. \end{aligned} \quad (24)$$

In the first line, the factors $\Delta(t_{\min}, t)$ and $\Delta(t, t_{\max})$ give the probabilities for no splittings to happen in the intervals $[t_{\min}, t]$ and $(t, t_{\max}]$, respectively. The splitting kernel $P_{\chi \rightarrow \chi}(x)$ describes the probability that a splitting happens at virtuality t . For two splittings, we have in analogy

$$\begin{aligned} p_2 &= \left(\frac{\alpha_{A'}}{2\pi} \right)^2 \int_{x_{\min}}^{x_{\max}} dx \int_{t_{\min}}^{t_{\max}} \frac{dt}{t} \int_{x_{\min}}^{x_{\max}} dx' \int_{t_{\min}}^t \frac{dt'}{t'} \Delta(t_{\min}, t) P_{\chi \rightarrow \chi}(x) \Delta(t, t') P_{\chi \rightarrow \chi}(x') \Delta(t', t_{\max}) \\ &\simeq e^{-\langle n_{A'} \rangle} \frac{1}{2!} \left(\frac{\alpha_{A'}}{2\pi} \right)^2 \int_{x_{\min}}^{x_{\max}} dx \int_{t_{\min}}^{t_{\max}} \frac{dt}{t} \int_{x_{\min}}^{x_{\max}} dx' \int_{t_{\min}}^{t_{\max}} \frac{dt'}{t'} P_{\chi \rightarrow \chi}(x) P_{\chi \rightarrow \chi}(x') \\ &= e^{-\langle n_{A'} \rangle} \frac{\langle n_{A'} \rangle^2}{2!}. \end{aligned} \quad (25)$$

In the second line, we have extended the integration region of the t' integral to the full range $[t_{\min}, t_{\max}]$ and included a factor $1/2!$ to compensate for the double counting induced that way. This is the place where the approximations discussed in sec. III A are crucial: extending the integration interval is only possible if we can assume that x_{\min} , x_{\max} , t_{\min} and t_{\max} are the same for all splittings and that $P_{\chi \rightarrow \chi}$ is independent of t . Eq. (25) straightforwardly generalizes to larger numbers of splittings, yielding the Poisson probabilities p_m in eq. (22).

C. Recursion relation for the χ and A' energy spectra

Let us now study the energy distributions of χ and A' in events with radiation of multiple A' bosons. Our starting point is the observation that, in the collinear limit, each splitting process is independent. As explained in sec. III A, we will make the crucial approximation that the integration boundaries x_{\min} , x_{\max} , t_{\min} , t_{\max} are the same for each emission process and are given by eqs. (15), (18) and (19) (with $E \rightarrow E_0$). We moreover neglect again the t -dependence of the splitting kernel $P_{\chi \rightarrow \chi}$. These approximations will allow us to compute the energy distributions recursively.

If we call the final energy of the on-shell DM particle after final state radiation E_χ and the energy fraction retained by the DM particle after all splittings $X \equiv E_\chi/E_0$,² we can write the final

² We use capital letters to denote quantities normalized to the initial energy E_0 of the DM particle before the first splitting, and lower case letters for quantities normalized to the energy of the DM particle as it enters a particular splitting process during the development of the A' shower.

DM energy distribution as

$$f_\chi(X) = \sum_{m=0}^{\infty} p_m f_{\chi,m}(X), \quad (26)$$

where $f_{\chi,m}(X)$ is the energy distribution of χ in events with exactly m emitted dark photons. $f_{\chi,m}(X)$ obeys the recursion relation (see also [57])

$$f_{\chi,m+1}(X) = \int_{x_{\min}}^{x_{\max}} dx_m f_{\chi,1}(x_m) \frac{f_{\chi,m}(X/x_m)}{x_m} \Theta(x_{\min} \leq X \leq x_{\max}), \quad (27)$$

where

$$f_{\chi,1}(X) \equiv \frac{1}{\langle n_{A'} \rangle} \frac{\alpha_{A'}}{2\pi} \int_{t_{\min}}^{t_{\max}} \frac{dt}{t} P_{\chi \rightarrow \chi}(X) \Theta(x_{\min} \leq X \leq x_{\max}), \quad (28)$$

is the energy fraction for dark radiation showers with only a single splitting and $\Theta(\cdot)$ denotes a window function that is 1 when the condition in parentheses is satisfied and 0 otherwise. Note that for $m = 1$, the definitions of x as the fraction of energy the DM particle retains in a single splitting and of X as the fraction of energy the DM particle retains after *all* splittings are identical. For $m = 0$, we define $f_{\chi,0}(X) \equiv \delta(1 - X)$. Note that $f_{\chi,m}(X)$ is normalized according to the condition

$$\int dX f_{\chi,m}(X) = 1. \quad (29)$$

When evaluating $f_\chi(X)$ numerically, we truncate the recursive series at $m = 10$, which is justified by the fact that the Poisson probability p_m is very small at $m \gg \langle n_{A'} \rangle$.

The distribution of the energy $E_{A'}$ of radiated A' bosons can be obtained in a similar way. With the notation $Z = E_{A'}/E_0$, it is given by

$$f_{A'}(Z) = \frac{1}{\langle n_{A'} \rangle} \sum_{m=1}^{\infty} \sum_{k=1}^m p_m f_{A',k}(Z), \quad (30)$$

where $f_{A',k}(Z)$ is the energy distribution of the k -th emitted A' boson. Note that $f_{A',k}(Z)$ is not a function of the total number of radiated dark photons m because each splitting process is independent. The recursion relation for $f_{A',k}(Z)$ is

$$f_{A',k+1}(Z) = \int_{x_{\min}}^{x_{\max}} dx_k f_{\chi,1}(x_k) \frac{f_{A',k}(Z/x_k)}{x_k} \Theta(1 - x_{\max} \leq Z \leq 1 - x_{\min}). \quad (31)$$

D. Energy spectra from an inverse Mellin transform

A particularly elegant way of computing the energy spectrum $f_\chi(X)$ of dark matter particles and the spectrum $f_{A'}(Z)$ of dark photons is by first computing the moments $\langle X^s \rangle$ and $\langle Z^s \rangle$ of these distributions, and then applying an inverse Mellin transform to recover $f_{A'}(Z)$ itself. The Mellin transform of a function $f(X)$ is defined as [58]

$$\mathcal{M}[f](s) \equiv \varphi(s) \equiv \int_0^\infty dX X^{s-1} f(X), \quad (32)$$

and the inverse transform is given by

$$f(X) = \frac{1}{2\pi i} \int_{c-i\infty}^{c+i\infty} ds X^{-s} \varphi(s). \quad (33)$$

The Mellin transform and its inverse are closely related to the Fourier and Laplace transforms [58] and can therefore be evaluated efficiently using the FFT (Fast Fourier Transform) algorithm [59].

For events in which a single A' is emitted, the moments of the DM energy distribution after the emission, weighted by the probability of having exactly one emission, are given by

$$\begin{aligned} p_1 \langle X^s \rangle_{1A'} &= e^{-\langle n_{A'} \rangle} \frac{\alpha_{A'}}{2\pi} \int_{x_{\min}}^{x_{\max}} dx x^s \int_{t_{\min}}^{t_{\max}} \frac{dt}{t} P_{\chi \rightarrow \chi}(x) \\ &\equiv e^{-\langle n_{A'} \rangle} \langle n_{A'} \rangle \overline{X^s}. \end{aligned} \quad (34)$$

In the last line, we have defined

$$\overline{X^s} \equiv \frac{1}{\langle n_{A'} \rangle} \frac{\alpha_{A'}}{2\pi} \int_{x_{\min}}^{x_{\max}} dx x^s \int_{t_{\min}}^{t_{\max}} \frac{dt}{t} P_{\chi \rightarrow \chi}(x). \quad (35)$$

As in the previous section, we again take x_{\min} , x_{\max} , t_{\min} and t_{\max} to have the same value for each splitting process, and we neglect the t -dependence of $P_{\chi \rightarrow \chi}$. If two A' bosons are emitted, we obtain analogously

$$\begin{aligned} p_2 \langle X^s \rangle_{2A'} &= e^{-\langle n_{A'} \rangle} \left(\frac{\alpha_{A'}}{2\pi} \right)^2 \int_{x_{\min}}^{x_{\max}} dx x^s \int_{t_{\min}}^{t_{\max}} \frac{dt}{t} \int_{x_{\min}}^{x_{\max}} dx' x'^s \int_{t_{\min}}^t \frac{dt'}{t'} P_{\chi \rightarrow \chi}(x) P_{\chi \rightarrow \chi}(x') \\ &\simeq e^{-\langle n_{A'} \rangle} \frac{1}{2!} \left(\frac{\alpha_{A'}}{2\pi} \right)^2 \int_{x_{\min}}^{x_{\max}} dx x^s \int_{t_{\min}}^{t_{\max}} \frac{dt}{t} \int_{x_{\min}}^{x_{\max}} dx' x'^s \int_{t_{\min}}^{t_{\max}} \frac{dt'}{t'} P_{\chi \rightarrow \chi}(x) P_{\chi \rightarrow \chi}(x') \\ &= e^{-\langle n_{A'} \rangle} \frac{\langle n_{A'} \rangle^2}{2!} \overline{X^s}^2. \end{aligned} \quad (36)$$

In the second line, we have again used the approximations from sec. III A to extend the integration region of the t' integral (see the discussion below eq. (25)). Eq. (36) can be easily generalized to the case of m emitted A' bosons:

$$p_m \langle X^s \rangle_{mA'} = e^{-\langle n_{A'} \rangle} \frac{\langle n_{A'} \rangle^m}{m!} \overline{X^s}^m. \quad (37)$$

Summing over m , we find the moments of the overall A' energy distribution:

$$\varphi(s+1) \equiv \langle X^s \rangle = \sum_{m=0}^{\infty} p_m \langle X^s \rangle_{mA'} = e^{-\langle n_{A'} \rangle(1-\overline{X^s})}. \quad (38)$$

An inverse Mellin transform of $\varphi(s)$ then yields the dark matter energy spectrum $f_{\chi}(X)$. As can be seen from eq. (33), this requires evaluating $\varphi(s)$ at complex values of s . A numerically stable way of doing this is by using the FFT algorithm to compute $\overline{X^s}$ (eq. (35)), then using eq. (38), and afterwards apply another FFT to evaluate the inverse Mellin transform.

The procedure for obtaining the A' spectrum is alike and yields for the contribution of showers with m dark photons to the moment s , weighted by the probability of emitting exactly m dark photons,

$$p_m \langle Z^s \rangle_{mA'} = \frac{1}{\langle n_{A'} \rangle} e^{-\langle n_{A'} \rangle} \frac{\langle n_{A'} \rangle^m}{m!} \overline{Z^s} \sum_{k=1}^m \overline{X^s}^{k-1}, \quad (39)$$

with

$$\overline{Z^s} \equiv \frac{1}{\langle n_{A'} \rangle} \frac{\alpha_{A'}}{2\pi} \int_{x_{\min}}^{x_{\max}} dx (1-x)^s \int_{t_{\min}}^{t_{\max}} \frac{dt}{t} P_{\chi \rightarrow \chi}(x). \quad (40)$$

Summing over all emissions we obtain

$$\langle Z^s \rangle = \frac{\overline{Z^s}}{\langle n_{A'} \rangle} \frac{1 - e^{-\langle n_{A'} \rangle(1-\overline{X^s})}}{1 - \overline{X^s}}. \quad (41)$$

An inverse Mellin transform yields the A' spectrum $f_{A'}(Z)$.

m_χ [GeV]	$m_{A'}$ [GeV]	$2 \langle n_{A'} \rangle$	$2 \langle n_{A'} \rangle_{\text{Pythia}}$	$\langle X \rangle$	$\langle X \rangle_{\text{Pythia}}$	$\langle Z \rangle$	$\langle Z \rangle_{\text{Pythia}}$	
A	50	1.5	2.130	2.340	0.873	0.837	0.119	0.140
	50	0.4	2.848	3.084	0.871	0.835	0.091	0.107
	4	1.5	3.476	3.540	0.729	0.697	0.156	0.171
	4	0.4	4.990	4.825	0.712	0.681	0.116	0.132
B	0.4	0.4	5.691	5.215	0.626	0.608	0.132	0.150

TABLE II: Characteristics of the dark photon shower for various choices of the DM mass m_χ and the dark photon mass $m_{A'}$. The rows labeled “A” and “B” correspond to the two benchmark points from table I. In all cases, we assume χ pair production at a center of mass energy $\sqrt{s} = 1$ TeV and we take $\alpha_{A'} = 0.2$. We show the predicted number $2 \langle n_{A'} \rangle$ of dark photons per event (with the factor of 2 coming from the fact that we consider χ pair production), the average fraction $\langle X \rangle$ that a χ particle retains of its initial energy after showering, and the average fraction $\langle Z \rangle$ of the initial χ energy that each dark photon receives. We compare the predictions of our semi-analytic calculations, eqs. (21), (38) and (41) (with $s = 1$), to the results of a Monte Carlo simulation in Pythia. As expected, the results satisfy the relation $\langle X \rangle + \langle n_{A'} \rangle \langle Z \rangle = 1$.

E. Comparison of analytic results to Monte Carlo simulations

We have also simulated the radiation of A' bosons fully numerically in Pythia 8 [35–37], using the “hidden valley” model implemented therein. Note that, like our analytic calculations, also the dark photon shower implemented in Pythia includes only dark photon radiation, $\chi \rightarrow \chi A'$ and $\bar{\chi} \rightarrow \bar{\chi} A'$, not dark photon splitting, $A' \rightarrow \bar{\chi}\chi$.

To compare the χ and A' energy spectra obtained using the different approaches, we assume χ pair production at a center of mass energy of $\sqrt{s} = 1$ TeV. In Pythia, this is achieved by simulating the process $e^+e^- \rightarrow Z' \rightarrow \bar{\chi}\chi$, followed by the dark photon shower. The results for several characteristic parameters of the dark parton shower, namely $\langle n_{A'} \rangle$, $\langle X \rangle$ and $\langle Z \rangle$, are shown in table II. Comparing Pythia results to the results obtained using eqs. (21), eq. (38) (with $s = 1$) and eq. (41) (with $s = 1$), we find excellent agreement. We attribute the remaining differences to the approximations we had to make in the analytical calculation, in particular the assumption that the upper and lower integration limits in x and t do not depend on x and t themselves.

A more detailed comparison between our analytic results and Pythia is shown in figs. 4 and 5. In fig. 4, we have plotted the distribution of the number of emitted dark photons per event (i.e. per $\bar{\chi}\chi$ pair) at our two benchmark points from table I. Fig. 5 shows the energy spectra of χ and A' after the dark photon shower has developed.

As we can see in fig. 4, Pythia results confirm that dark photon emission is approximately a Poisson process. We attribute the small deviations to the approximations we made in deriving eq. (22) in sec. III B.

Regarding the energy spectra plotted in fig. 5, we find excellent agreement between both of our analytic approaches (red dashed and blue dot-dashed curves) and also with Pythia results (black dashed curves). Note that the recursive method is numerically less stable than the Mellin transform approach because numerical errors—especially those incurred close to the upper integration boundary x_{\max} at which the splitting kernel has a regularized singularity—can accumulate in the recursive formulas (27) and (31). We have also carried out simple leading order simulations of the processes $e^+e^- \rightarrow Z' \rightarrow \bar{\chi}\chi$ and $e^+e^- \rightarrow Z' \rightarrow \bar{\chi}\chi A'$ in CalcHEP [60] (gray solid curves in fig. 5) and find that, as expected, this simulation reproduces our analytic result for the specific process $e^+e^- \rightarrow Z' \rightarrow \bar{\chi}\chi A'$ very well, but is insufficient as a proxy for the full dark photon spectrum. Since the full dependence of the matrix element on m_χ and $m_{A'}$ is taken into account in CalcHEP, it also illustrates that the approximations discussed in sec. III A are justified at this level. In

↗ probability
curve

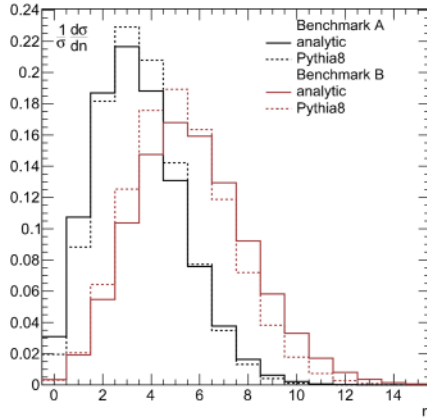


FIG. 4: The distribution of the number n of dark photons emitted in each $\bar{\chi}\chi$ pair production event at a center of mass energy of $\sqrt{s} = 1$ TeV. The model parameters are given in table I. The solid curves labeled “analytic” show the Poisson probability $e^{-2\langle n_{A'} \rangle} [2\langle n_{A'} \rangle]^n / n!$, with $\langle n_{A'} \rangle$ given by eq. (21). The factors of 2 arise from the fact that two DM particles are produced in each event. The dotted curves show the distribution obtained from a Monte Carlo simulation of the dark photon shower in Pythia.

fig. 5, we also show the contributions $p_m f_{\chi,m}(X)$ and $(1/\langle n_{A'} \rangle) \sum_{k=1}^m p_m f_{A',k}(Z)$ from events with a particular fixed number of dark photons to the overall energy spectra $f_\chi(X)$ and $f_{A'}(Z)$ (dashed rainbow-colored curves). Note that events with several emitted A' bosons can dominate over events with a single A' because $2\langle n_{A'} \rangle > 1$ at our benchmark points. This illustrates that the A' spectrum would be very difficult to obtain from a full matrix element calculation and necessitates a parton shower algorithm.

In summary, we have developed in this section two analytic methods for computing the energy spectrum of χ and A' , and we have verified them by comparing to Monte Carlo simulations.

IV. COLLIDER SEARCHES FOR LEPTON JETS FROM DARK RADIATION

To constrain radiating DM models using existing LHC lepton jet searches, we numerically simulated the expected signal and background event spectra at center of mass energies of $\sqrt{s} = 7$ TeV and $\sqrt{s} = 8$ TeV. As in sec. III E, signal events are generated using the implementation of a “hidden valley” model in Pythia 8 [35–37]. We compare our simulation results to data from a 7 TeV ATLAS search for prompt lepton jets [15] and from an 8 TeV ATLAS search for displaced lepton jets [16]. We have also simulated events at $\sqrt{s} = 13$ TeV to predict the sensitivity of future searches for prompt and displaced lepton jets.

A. Prompt lepton jets

Our prompt lepton jet analysis follows the 7 TeV, 5 fb^{-1} ATLAS search in ref. [15], but including only muonic lepton jets. The reason for discarding lepton jets with electrons is that it is very difficult to implement the corresponding selection criteria without a full detector simulation. The trigger requirement for muonic lepton jets is the presence of either three muons with transverse momenta $p_T > 6$ GeV or one muon with $p_T > 18$ GeV. Muons are required to have pseudorapidity $|\eta| < 2.5$, and they are required to have a track in the inner detector associated with them. We

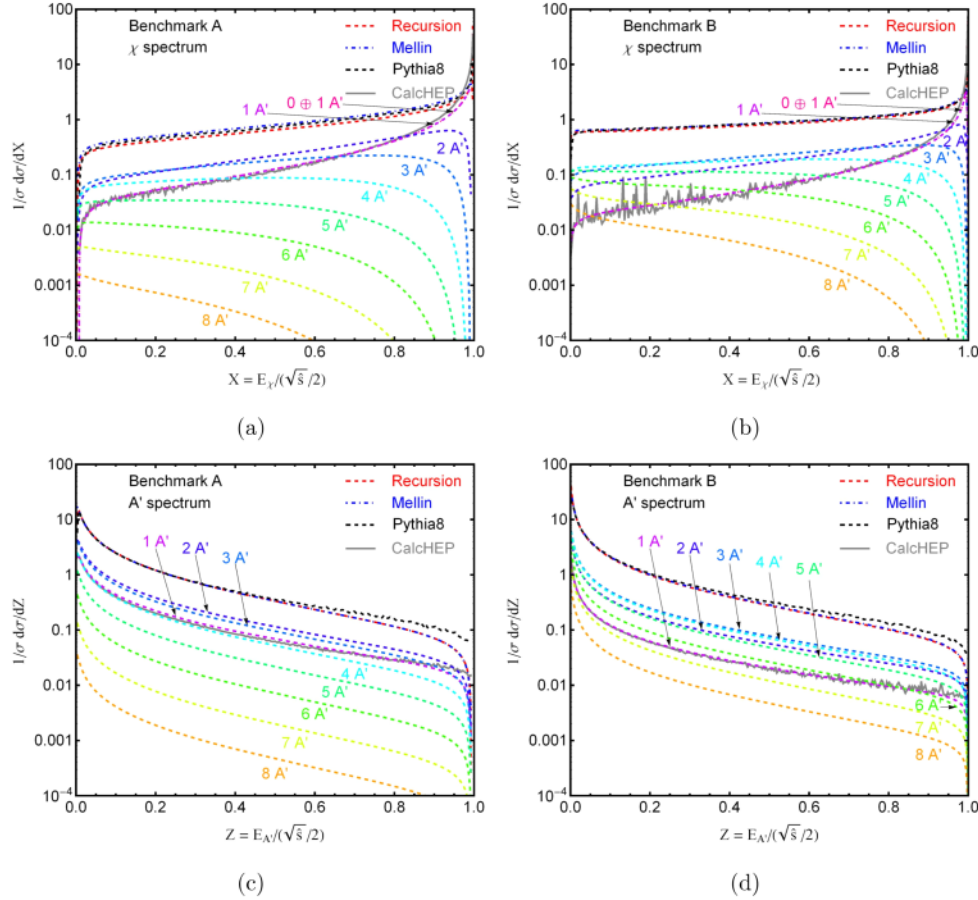


FIG. 5: (a), (b) Energy spectrum $f_\chi(X)$ of DM particles χ after final state radiation; (c), (d) energy spectrum $f_{A'}(Z)$ of dark photons A' emitted as final state radiation. The panels on the left are for benchmark point A from table I, the panels on the right are for benchmark point B. In all cases, we assume χ pair production at a center of mass energy $\sqrt{s} = 1$ TeV. We compare the results from the recursion formulas described in sec. III C, the Mellin transform method developed in sec. III D, the dark photon shower simulation in Pythia, and a simple leading order simulation of $e^+e^- \rightarrow Z' \rightarrow \bar{\chi}\chi A'$ in CalcHEP. For the Mellin transform method, we also show the result separated according to the number of A' bosons emitted in each $\bar{\chi}\chi$ pair production event.

implement the last requirement by demanding that the parent A' of the muon decays within a radius of 122.5 mm (corresponding to the position of the last silicon pixel layer) from the beam axis. Finally, muon tracks are required to have a transverse impact parameter $|d_0| < 1$ mm with respect to the primary vertex.

We cluster muons into lepton jets using the following algorithm: we collect all muons with a cone of radius $\Delta R = 0.1$ around the highest- p_T muon in the event to form the first lepton jet. We then iterate this procedure, starting, in each iteration, with the highest- p_T muon not associated with a lepton jet yet. Ref. [15] then defines two classes of events that are considered in the analysis:

Double muon jet events require at least two muonic lepton jets, each of which must contain at least two muons with $p_T > 11$ GeV. If the event was selected only by the single muon trigger, the leading muon in the lepton jet is in addition required to have $p_T > 23$ GeV. Moreover, the two muons closest in p_T within each lepton jet are required to have an invariant mass $m_{\mu\mu} < 2$ GeV.

To reject non-isolated lepton jets, the variable

$$\rho \equiv \frac{\sum_i E_{T,i}}{p_{T,\text{LJ}}}, \quad (42)$$

is defined, where the sum in the numerator runs over the E_T of all calorimeter deposits within $\Delta R = 0.3$ of any muon in the lepton jet, but excluding deposits within $\Delta R < 0.05$ around any muon. The denominator is the p_T of the lepton jet. The isolation cut imposes $\rho < 0.3$.

Single muon jet events require only one muonic lepton jet, but this lepton jet must contain at least four muons with $p_T > 19$ GeV, 16 GeV, 14 GeV for the three leading muons and $p_T > 4$ GeV for all other muons. The same invariant mass cut as for the double muon jet analysis is imposed, and the isolation variable (42) has to satisfy $\rho < 0.15$.

Since we find that double muon jet events are much more sensitive to our radiating DM model than single muon jet events, we do not include the latter in the following analysis.

The dominant background to the muonic lepton jet search is from misidentified QCD multijet events, which contribute 0.5 ± 0.3 events in the signal region [15]. For the 7 TeV analysis, we can use this number at face value, while for the extrapolation to $\sqrt{s} = 13$ TeV, we assume the background cross section after cuts to be a factor of 3 larger. This factor of 3 corresponds roughly to the scaling of the cross section for QCD jet production [61]. We assume the relative error on the background to remain the same as at 7 TeV. Note that, to be able to use this simple scaling of the background cross section, we have to use the same cuts at 7 TeV and at 13 TeV.

B. Displaced lepton jets

Our search for displaced lepton jets, based on the ATLAS 8 TeV, 20.3 fb^{-1} analysis [16], is somewhat more involved than the search for prompt lepton jets described in the previous section. First, we need to be more careful in simulating detector effects, which we do at particle level. We pay particular attention to the displaced A' decay vertices, which lead to unusual detector signatures for each particle. The coordinates of the A' decay vertex and the momenta of the A' decay products are smeared by Gaussians with widths proportional to $1/L_{xy}$, where L_{xy} is the transverse distance of the A' decay vertex from the beam pipe. This way, we in particular take into account the fact that the momenta of charged particles that travel through more material are affected more strongly by the smearing. All parameters of our detector simulation are calibrated against the lepton jet reconstruction efficiencies shown in fig. 6 of ref. [16]. Since this plot is for a sample of dark photons with flat p_T and η distributions in the range $p_T \in [10, 100]$ GeV and $\eta \in [-2.5, 2.5]$, we generated a similar event sample for the comparison. To further improve the agreement between our predicted efficiencies and the results from ref. [16], we apply a fudge factor in each L_{xy} bin.

Following [16], muons are selected from the event sample if they are produced inside the sensitive ATLAS detector volume, i.e. up to a radius of 7 m. Only loose requirements on the transverse momentum and pseudo-rapidity of reconstructed muons are applied: their p_T must be above the trigger threshold of 6 GeV and the pseudorapidity $|\eta|$ must be < 2.5 . Since the goal of the search in ref. [16] was to constrain long-lived dark photons with displaced decay vertices, the background from prompt muons is reduced by requiring stand-alone muons, i.e. muons that are detected in the muon spectrometer but cannot be matched to a track in the inner detector. This essentially means that the dark photon decay in which the muon was produced must have happened outside the last pixel layer of the inner detector (ID), located at a radius of 122.5 mm from the beam pipe. To suppress cosmic ray muons, the reconstructed muon trajectory must still be associated with the primary interaction vertex. In particular, it must fulfill requirements on the impact parameters $|z_0| < 270$ mm (longitudinal) and $|d_0| < 200$ mm (transverse).

Hadronic jets (or, more precisely, calorimeter jets) are based on energy deposits in the electromagnetic calorimeters (ECAL) and hadronic calorimeters (HCAL), clustered using the anti- k_T algorithm [62] implemented in FASTJET [63] with a cone radius of $R = 0.4$. Calorimeter jets must fulfill $p_T > 20$ GeV and $|\eta| < 2.5$.

Three different types of lepton jets (LJ) are defined: A type-0 or “muonic” LJ arises from dark photon showers in which all A' bosons decay to muons. It consists of at least two displaced and collimated muons with no additional activity nearby. If however, such muons are accompanied by a single calorimeter jet, we call the sum of these objects a type-1 or “mixed” LJ. A type-2 LJ or “calorimeter” LJ is defined as an isolated calorimeter jet that fulfills additional requirements to distinguish it from QCD background. Note that, especially for type-1 and type-2 LJs, the term lepton jet used in [16] is somewhat misleading because these objects can also arise from hadronic A' decays. The clustering algorithm for all three LJ types is described in the following.

We collect all muons and calorimeter jets inside a cone of radius $\Delta R = 0.5$ around the highest- p_T muon in the event. If at least one other muon and no calorimeter jet is found inside this cone, those muons are combined to a muonic LJ. If at least one muon and exactly one calorimeter jet is found inside the cone, all objects are combined into a mixed LJ. If no second muon is found within $\Delta R = 0.5$ of the highest- p_T muon, the muon is discarded. The algorithm then continues with the highest- p_T muon that has not been associated with a lepton jet or discarded yet. After all muons have been processed, the remaining calorimeter jets are reconstructed as calorimeter LJs if their electromagnetic (EM) fraction is lower than 0.1. This is for example true for dark photons decaying to charged pions, but also for decays to electrons happening inside the hadronic calorimeter. Since the pseudo-rapidity region $1.0 < |\eta| < 1.4$ tends to create a fake low EM fraction due to the transition between the barrel and endcap EM calorimeters (ECAL), this region is excluded. Additionally the width W of a calorimeter LJ, defined by

$$W \equiv \frac{\sum_i \Delta R^i \cdot p_T^i}{\sum_i p_T^i} < 0.1, \quad (43)$$

needs to be small. Here, the sum runs over all particles in the lepton jet. An isolation cut is imposed on all reconstructed lepton jets by requiring that the scalar p_T sum of all charged tracks, reconstructed by the inner detector inside a cone of radius 0.5 around the lepton jet axis, is below 3 GeV. Only charged tracks with $p_T > 400$ MeV and with impact parameters $|z_0| < 10$ mm and $|d_0| < 10$ mm are considered in this procedure. An event is discarded if there are not exactly two lepton jets fulfilling $|\Delta\phi| > 1.0$. The requirement of two lepton jets leads to the 6 different combinations 0–0, 0–1, 0–2, 1–1, 1–2, and 2–2, where e.g. 0–1 corresponds to an event reconstructed with one type-0 (muonic) and one type-1 (mixed) lepton jet.

The sensitivity of the displaced analysis will depend strongly on the A' decay mode. Therefore, we list in table III the most important A' decay modes and their associated signatures. Check marks (\checkmark) indicate in which region of the detector a particular decay has to happen in order to potentially be reconstructed as a displaced lepton jet. For decays that would fail our cuts, we give the reason why they are vetoed. For instance, due to the requirement of a low EM fraction, $A' \rightarrow e^+e^-$ is only identified as a displaced lepton jet if the decay happens inside the hadronic calorimeter, while $A' \rightarrow \mu^+\mu^-$ is also selected if the decay happens inside the electromagnetic calorimeter. Decays to any final states involving charged particles are vetoed if they happen in the inner detector. Regarding decays to mesons, it is important to note that π^\pm , K^\pm and K_L^0 have lifetimes of order 10^{-8} sec [64] and are thus stable on detector scales (i.e. they will be stopped in the hadronic calorimeter before they decay). Neutral pions, on the other hand, decay very fast. For K_S^0 , the lifetime of 9×10^{-11} sec may allow it to travel for several cm before decaying (mostly to $\pi^+\pi^-$ or $\pi^0\pi^0$). Therefore, $A' \rightarrow \pi^+\pi^-$, K^+K^- are accepted if they happen in the electromagnetic or hadronic calorimeter. The decay $A' \rightarrow \pi^+\pi^-\pi^0$, on the other hand is vetoed if it happens in the electromagnetic calorimeter because the quasi-instantaneous decay of the π^0 to two photons

Detector	$A' \rightarrow e^+e^-$	$A' \rightarrow \mu^+\mu^-$	$A' \rightarrow \pi^+\pi^-/K^+K^-$	$A' \rightarrow \pi^+\pi^-\pi^0$	$A' \rightarrow K_L^0 K_S^0$
LJ type	2 (calorimeter)	0 (muonic)	2 (calorimeter)	2 (calorimeter)	2 (calorimeter)
ID	track	track	track	track	(✓)
ECAL	EM fraction	✓	✓	EM fraction	(✓)
HCAL	✓	✓	✓	✓	✓

TABLE III: Illustration of where in the detector a specific A' decay must happen in order to potentially be reconstructed as a lepton jet in our displaced lepton jet analysis (see sec. IV B and ref. [16]. For decays that will be vetoed, a reason for the veto is given. The type of lepton jet as which each decay mode is most likely to be reconstructed is given at the top of the table.

deposits a large amount of energy, violating the cut on the EM fraction. The decay $A' \rightarrow K_L^0 K_S^0$ is successfully reconstructed as a displaced lepton jet in many, but not all, cases. It will be vetoed in the inner detector if both the A' and the secondary K_S^0 decay very fast (well within the 12.25 cm radius of the inner detector) in spite of their typically large boosts, and the K_S^0 decay mode is to $\pi^+\pi^-$ (branching ratio 69%). It will be vetoed by the cut on the EM fraction if the A' decay happens in the inner detector or the electromagnetic calorimeter and the K_S^0 decay mode is to $\pi^0\pi^0$ (branching ratio 31%).

Note that, as can be read from table III, the decay mode $A' \rightarrow \mu^+\mu^-$ is most likely to be reconstructed as a type-0 (muonic) lepton jet, while all other decay modes typically lead to type-2 (calorimeter) lepton jets. Type-1 (mixed) lepton jets are obtained only if several A' are radiated from the same dark matter particle, with at least one of them decaying to $\mu^+\mu^-$ and at least one of them decaying to a different final state. Therefore, the requirement for a type-1 (mixed) lepton jet are the most difficult to satisfy. The predicted signal event numbers in table. V confirm this.

C. Results

In tables IV and V we present the signal and background predictions as well as the observed event numbers for the two benchmark models defined in table I. Table IV is for the prompt lepton jet analysis from ref. [15], using 5 fb^{-1} of 7 TeV ATLAS data (see sec. IV A, while table V is for the displaced lepton jet search from ref. [16], using 20.3 fb^{-1} of 8 TeV ATLAS data (see sec. IV B). Note that, for the prompt search, we include only muonic lepton jets, which are easier to model without a full detector simulation. For the displaced search, we show event numbers with and without inclusion of the background-limited sample of events with two type-2 lepton jets. We see from tables IV and V that, as expected, benchmark point A is more easily detectable in the displaced search, while benchmark point B is probed more sensitively by the prompt search.

We also show our predictions for 100 fb^{-1} of 13 TeV data. In general, we expect better sensitivity at 13 TeV because of the larger integrated luminosity expected. Since an estimation of the multijet background at 13 TeV is problematic, we restrict the displaced lepton jet search at 13 TeV to type-0 (muonic) LJs, for which QCD backgrounds do not play a major role. The only relevant source of background in the 13 TeV displaced search are then cosmic rays, whose flux is independent of the collider center of mass energy as long as we use the same cuts as at $\sqrt{s} = 8 \text{ TeV}$. Our predictions for the sensitivity of a displaced lepton jet search at 13 TeV LHC are thus very conservative. For the prompt search at 13 TeV, we scale the background cross section from the 7 TeV analysis by a factor of 3.

We use the CLs method [65] to compare our predictions at $\sqrt{s} = 7 \text{ TeV}$ and $\sqrt{s} = 8 \text{ TeV}$ to the data and to constrain the production cross section for a DM pair, $\sigma(pp \rightarrow Z')\text{BR}(Z' \rightarrow \bar{\chi}\chi)$. We use the ATLAS background predictions [15, 16] as the null hypothesis, and the sum of the ATLAS

	7 TeV	13 TeV
Benchmark A	0.8	109
Benchmark B	3.9	334
All backgrounds	0.5 ± 0.3	30 ± 18
data	3	

TABLE IV: Predicted event rates for the prompt lepton jet analysis (see sec. IV A and ref. [15]) at the benchmark parameter points from table I, compared to the background predictions and the observed event rates from ref. [15].

	Lepton jet type							
	0-0	0-1	0-2	1-1	1-2	2-2	All	All excl. 2-2
Cosmic ray bkg.	15	0	14	0	0	11	$40 \pm 11 \pm 9$	$29 \pm 9 \pm 29$
8 TeV								
Multi-jet bkg.							$70 \pm 58 \pm 11$	$12 \pm 9 \pm 2$
Benchmark A	14	3	104	0	14	200	$335 \pm 18 \pm 100$	$135 \pm 12 \pm 41$
Benchmark B	2.1	0.4	3.0	0	0.3	1.2	$7 \pm 2.1 \pm 2.6$	$5.8 \pm 1.7 \pm 2.4$
data	11	0	11	4	3	90	119	29
13 TeV								
Benchmark A	169							
Benchmark B	28							

TABLE V: Predicted event rates for the displaced lepton jet analysis (see sec. IV B and ref. [16]) at the benchmark parameter points from table I, compared to the background predictions and the observed event rates from ref. [16]. In the last two columns, the first error is the statistical uncertainty, while the second one is systematic. Our sensitivity study at $\sqrt{s} = 13$ TeV includes only type 0-0 events (only muonic lepton jets) because a reliable extrapolation of the multijet background to 13 TeV is difficult.

background and our signal prediction as the test hypothesis. For $\sqrt{s} = 13$ TeV, we compare our signal+background prediction to the background-only prediction to obtain the expected limit. We assume a systematic uncertainty of 30% on the signal normalization to account for errors in the signal and detector simulation. The results are presented in figs. 6 and 7 for the two benchmark points from table I, where in each panel one of the model parameters is varied while the others are kept constant. For the displaced search at $\sqrt{s} = 8$ TeV, two different limits are calculated, one including all tagged events (solid red curves) and one excluding type 2–2 events, i.e. events with two type-2 lepton jets (solid black curves). Due to the larger background in the 2–2 sample, this second limit is stronger in certain parameter regimes than the limit including all lepton jets. For the displaced search at $\sqrt{s} = 13$ TeV, (red dotted curves), we use only events with two type-0 lepton jets, as explained above. We also show in figs. 6 and 7 the predicted values for $\sigma(pp \rightarrow Z')\text{BR}(Z' \rightarrow \bar{\chi}\chi)$ as thin dotted curves.

Let us first discuss fig. 6, corresponding to benchmark point A. (We will comment on the differences compared to fig. 7 below.) Since for fixed $m_{A'}$, the dark photon decay length $c\tau$ depends only on the kinetic mixing parameter ϵ , figs. 6 (a) and (b) are equivalent. We see that the best limits from the prompt search are obtained at $c\tau \lesssim 1$ mm ($\epsilon \gtrsim 10^{-5}$), while for larger decay length, the cut on the impact parameter $|d_0| < 1$ mm restricts the sensitivity. For the displaced search, the sensitivity is optimal around $c\tau = 10$ –100 mm, corresponding to $\epsilon \simeq \text{few} \times 10^{-6}$. For shorter lifetimes (larger ϵ) the dark photon decay vertices tend to be closer to the primary interaction

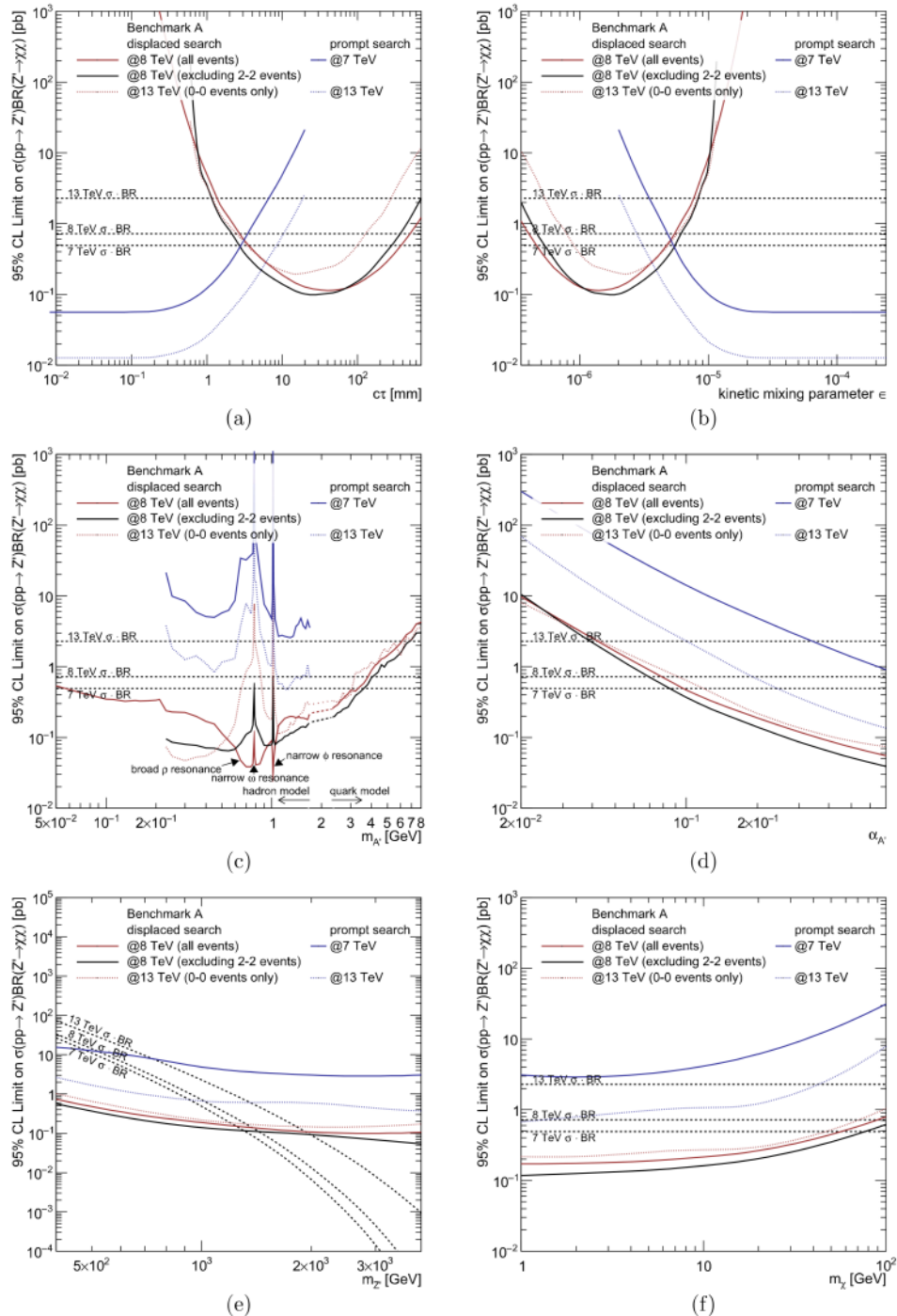


FIG. 6: 95% CL upper limits on the DM $DM + nA'$ production cross section as a function of the model parameters for benchmark point A from table I. In each panel, we vary one parameter while keeping the others fixed at their benchmark values. Exclusion limits from the 7 TeV ATLAS search for prompt lepton jets [15] (solid blue) and from the 8 TeV ATLAS search for displaced lepton jets [16] are shown. For the latter search, we show results including all lepton jet events (red solid) and excluding events with two type-2 lepton jets (black solid). The predicted sensitivity of similar analyses at $\sqrt{s} = 13$ TeV is shown as blue/red dotted curves. The black dotted lines in each panel show the theoretically predicted production cross sections.

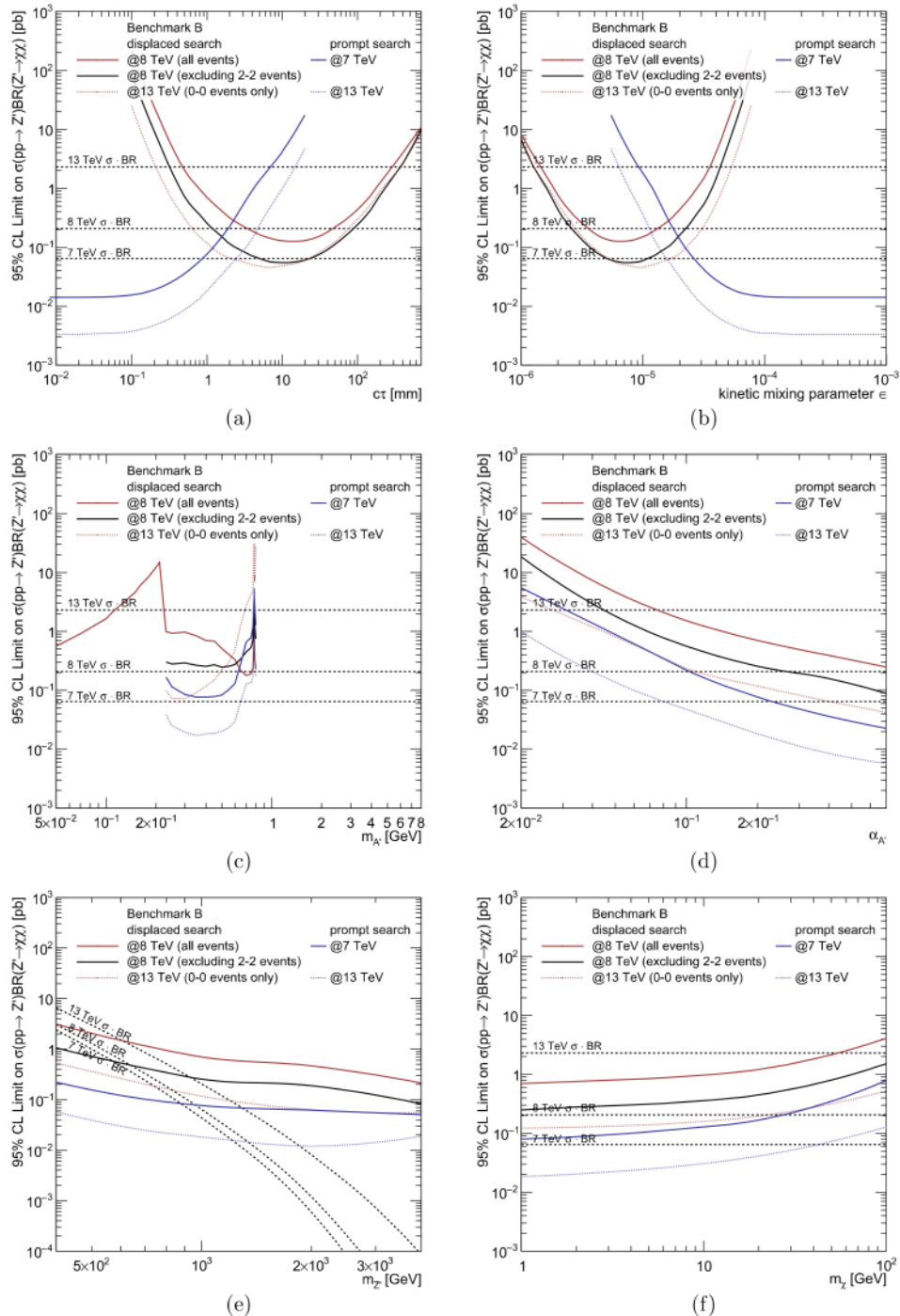


FIG. 7: Same as fig. 6, but for benchmark point B from table I.

point, so that the A' decay products are more likely to leave tracks in the inner detector, thus failing the displaced lepton jet selection criteria. For too large lifetimes (smaller ϵ), on the other hand, most dark photons will decay outside the ATLAS detector and not lead to a signal at all. The exact position of the most sensitive regime depends strongly on the A' kinematics and its mass.

For the displaced search, notice also the slight shift of the most sensitive point in $c\tau$ and ϵ between the red solid, black solid and red dotted curves in figs. 6 (a) and (b). This is related mostly to the inclusion/exclusion of different types of lepton jets in the three cases. In particular, as explained above, we include only type-0 (muonic) lepton jets in the 13 TeV analysis. The decay $A' \rightarrow \mu^+ \mu^-$ can be successfully reconstructed for shorter A' decay lengths than many other A' decay modes (see table III) Consequently, the exclusion limit based on displaced type 0–0 events only (red dotted curves in fig. 6 (a) in (b)) is best at relatively small $c\tau$ (relatively large ϵ), followed by the sample excluding type 2–2 events and by the sample including all types of lepton jets.

Similar arguments help us understand the exclusion limits as a function of the A' mass in fig. 6 (c). The different peaks and dips in this plot reflect the dependence of the A' decay branching ratios on $m_{A'}$ illustrated in fig. 2, see also [64]. The most notable features arise due to the broad ρ^0 resonance around 780 MeV with the narrow ω resonance on top of it and the narrow ϕ resonance at 1 GeV. The ρ^0 resonance decays almost exclusively to $\pi^+ \pi^-$ pairs, so that around this resonance, the relative importance of all other decay channels is diminished. This implies that the prompt lepton jet search, which includes only muonic lepton jets, has a greatly reduced sensitivity around the ρ resonance. In the displaced search, most $A' \rightarrow \rho^0 \rightarrow \pi^+ \pi^-$ decays are reconstructed as type 2 (calorimeter) lepton jets (see table III), therefore the sensitivity improves around the ρ^0 resonance if type 2–2 events are included in the analysis (red solid curve in fig. 6 (c)). If type 2–2 events are excluded (black solid and red dotted curves in fig. 6 (c)), the sensitivity decreases. The dominant decay of the ω resonance is to $\pi^+ \pi^- \pi^0$. This again decreases the sensitivity of the prompt search around the resonance. For the displaced search, we can read from table III that the decay $A' \rightarrow \omega \rightarrow \pi^+ \pi^- \pi^0$ is more likely to be vetoed than $A' \rightarrow \pi^+ \pi^-$, therefore the sensitivity is reduced at the ω resonance compared to the off-resonance region. The behavior at the ϕ resonance is similar to that at the ρ^0 resonance. The prompt search is insensitive because the ϕ mostly decays hadronically. For the displaced search, detection prospects for the dominant decay channel $\phi \rightarrow K^+ K^-$ (branching ratio 48.9%) as a type-2 (calorimeter) lepton jet are very similar to those of the ρ^0 resonance decaying to $\pi^+ \pi^-$ (see table III). The secondary decay $\phi \rightarrow K_L^0 K_S^0$ (branching ratio 34.2%) has a high probability of being reconstructed as a displaced type-2 lepton jet even if the A' decay happens in the inner detector. For these reasons, the sensitivity at the ϕ resonance is further boosted in analyses including displaced type-2 lepton jets. For A' masses above 1 GeV, the sensitivities of both the prompt and the displaced searches decrease rapidly. For the prompt search, the invariant mass requirement $m_{\mu\mu} < 2$ GeV restricts the realm of sensitivity to $m_{A'} < 2$ GeV. For the displaced search, the smaller A' boost factor at larger $m_{A'}$ implies that the A' decay length becomes shorter and events are more likely to leave tracks in the inner detector and be vetoed. Moreover, the average number of radiated A' decreases at larger $m_{A'}$. As discussed in sec. II, we do not consider the region $1.7 \text{ GeV} < m_{A'} < 2.3 \text{ GeV}$, where numerous hadronic resonances appear but the quark model is not applicable yet. In fig. 6 (c), we have smoothly interpolated through this region. As can be seen, the low-energy description in terms of hadron final states and the high-energy description in terms of quark final states match onto each other very well.

In fig. 6 (d), we find that, unsurprisingly, all limits improve as the dark sector gauge coupling $\alpha_{A'}$ increases because the probability for A' radiation grows. Note, however, that in the very large $\alpha_{A'}$ region, our perturbative treatment of the dark photon shower is expected to break down.

Concerning the dependence of the sensitivity on the Z' mass (fig. 7 (e)), we find that at $m_{Z'} < \text{few TeV}$, the sensitivity of all searches increases with $m_{Z'}$. This is because a heavier Z' decays to more energetic χ particles, which radiate more dark photons. Eventually, of course, on-shell

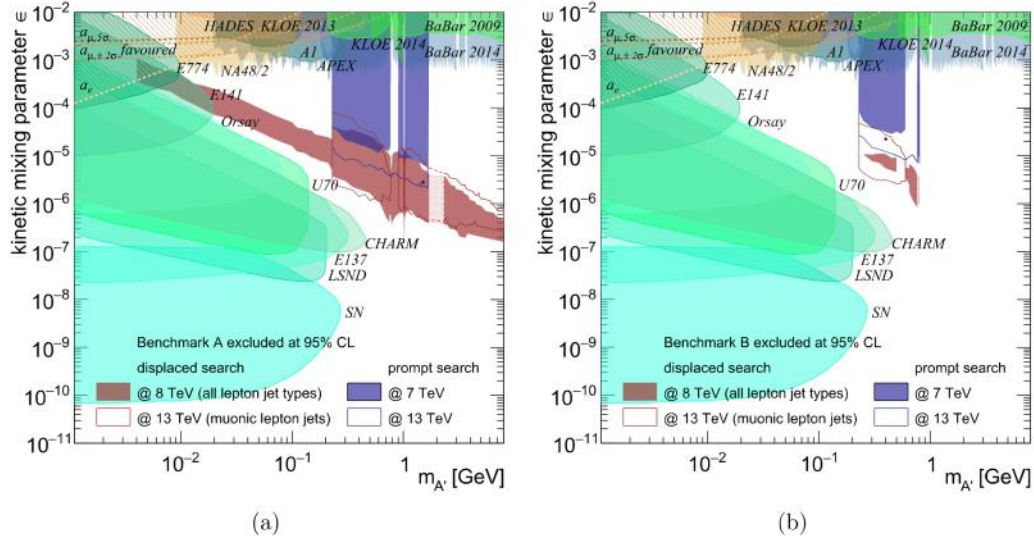


FIG. 8: 95% CL constraints on the dark photon mass $m_{A'}$ and the kinetic mixing parameter ϵ , with all other model parameters fixed at the first (second) set of benchmark values from table I in the left hand (right hand) panel. We show exclusion limits from the ATLAS search for prompt lepton jets in 5 fb^{-1} of 7 TeV data [15] (blue shaded region) and from their displaced lepton jet search in 20.3 fb^{-1} of 8 TeV data [16] (red shaded region), as well as projected sensitivities for 100 fb^{-1} of 13 TeV data (blue/red unshaded regions). Black stars correspond to the nominal values of $m_{A'}$ and ϵ from table I. The lighter colored region around $m_{A'} = 2 \text{ GeV}$ corresponds to the transition region between the analysis in terms of hadron final states and the analysis in terms of quark final states and is based on interpolation. We also show the existing 90% CL exclusion limits from the electron and muon anomalous magnetic moment [66–68], HADES [69], KLOE 2013 [70] and 2014 [71], the test run results from APEX [72], BaBar 2009 [73] and 2014 [74], beam dump experiments E137, E141, and E774 [75–77], A1 [78], Orsay [79], U70 [80], CHARM [81], LSND [82], as well as constraints from astrophysical observations [83, 84] and π^0 decays [85].

production of the Z' becomes impossible and the sensitivity decreases again.

Finally, fig. 6 (f) shows that the sensitivity goes down when χ is made heavier because less boosted χ particles radiate less.

Let us now turn to a comparison of the two benchmark models from table I and compare figs. 6 and 7. The general features of the two figures are very similar, but in general benchmark point B is more easily detectable in prompt lepton jet searches due to the smaller $c\tau$. Benchmark point B offers somewhat better sensitivity than benchmark point A also because the smaller values of m_χ and $m_{A'}$ imply that the average number of A' radiated in each event is larger. This effect is especially pronounced in the displaced searches excluding type 2–2 events, which are limited by backgrounds. Note that in fig. 7 (c) the region with $m_{A'} > 2m_\chi$ is not considered because it would lead to a very large branching ratio for $A' \rightarrow \bar{\chi}\chi$, making the A' invisible to the detector.

To put our results in the context of other constraints on dark photons, we show in fig. 8 the dark photon parameter space spanned by ϵ and $m_{A'}$. For both of our benchmark points, we compare the limits we derived from the prompt and displaced ATLAS lepton jet searches (blue shaded/red shaded) and the predictions for 13 TeV (blue/red unshaded) to the exclusion limits from various low energy experiments. For the 8 TeV displaced analysis, we decide for each parameter space point individually whether or not to exclude type 2–2 events (events with two calorimeter lepton jets), depending on which analysis leads to the better expected limit.

We see that the parameter region probed by LHC lepton jet searches is complementary to the

region probed by low energy searches. It is important to keep in mind, though, that low energy experiments probe any dark dark photon model, while our analysis is sensitive only to scenarios that, in addition, feature a light DM particle that can be pair-produced at the LHC. We see that benchmark point A is already excluded by the 8 TeV ATLAS search for displaced lepton jets, while benchmark point B can be probed by both the prompt and the displaced search at 13 TeV. The exclusion regions from the displaced searches move to smaller values of ϵ at larger $m_{A'}$ because the A' width increases and the lab frame decay length decreases with increasing $m_{A'}$ due to the smaller boost factors. Both effects need to be compensated by a decrease in ϵ to avoid A' decays in the inner detector. The impact of the various A' decay channels on the sensitivity is again reflected by spikes, dips and kinks in the excluded regions. For instance, note that the prompt search at 7 TeV, which includes only muonic lepton jets, is insensitive close to the hadronically decaying ρ , ω and ϕ resonances. At 13 TeV, the gap is closed thanks to the much better statistics. The sharp edge at low A' mass for the 7 TeV and 13 TeV regions corresponds to the opening of the decay channel $A' \rightarrow \mu^+ \mu^-$ at $m_{A'} = 2m_\mu$. Remember that, in our 7 TeV and 13 TeV analysis, we could only include muonic lepton jets, therefore, our analysis is insensitive below the muon threshold. A full experimental search would of course extend also into this region, like the 8 TeV ATLAS search for displaced lepton jets has done.

V. CONCLUSIONS

In summary, we have studied the possibility of revealing the properties of a dark sector of particle physics by using final state radiation from dark matter produced at the LHC. The characteristic experimental signature of this process is a pair of lepton jets. While our conclusions apply to a very large class of extended dark sector models, we have worked in the framework of a toy model where fermionic dark matter particles χ are charged under a new dark sector gauge group $U(1)'$ and coupled to the SM through a heavy mediator. When χ particles are pair-produced at the LHC via this heavy mediator, they can radiate several light $U(1)'$ gauge bosons A' (dark photons) which subsequently decay to light SM particles (electrons, muons, mesons) through a small kinetic mixing ϵ with the SM photon. Due to the required smallness of the kinetic mixing, the A' decay length can be macroscopic. We emphasize that our results for this toy model are easily generalized to any model with light dark sector particles charged under a new gauge interaction. We also remind the reader that, in order to account for all of the DM in the Universe, χ must be produced non-thermally, as for instance in asymmetric DM scenarios.

We have first developed two analytic treatments of dark photon radiation: in the first one, we use recursive expressions for the A' and χ energy distributions, while in the second one, we compute the moments of these distributions fully analytically and then apply an inverse Mellin transform to obtain the distributions themselves. We have compared our analytic calculations with Monte Carlo simulations in Pythia, finding excellent agreement.

In the second part of the paper, we have extended these Monte Carlo simulations by a simplified description of the ATLAS detector that allows us to recast the existing ATLAS searches for prompt and displaced lepton jets into powerful limits on the DM pair production cross section and the dark photon parameters in radiating DM models. Our limits on the $\bar{\chi}\chi$ production cross section range down to $\mathcal{O}(10\text{ fb})$, depending on the A' mass and lifetime, the $U(1)'$ gauge coupling, and the mass of χ . Regarding the A' properties, we find that LHC searches for radiating DM can probe a region in $m_{A'} - \epsilon$ space that has been inaccessible to low energy dark photon searches so far, namely in the parameter range $10^{-7} \lesssim \epsilon \lesssim 10^{-3}$ for $m_{A'}$ in the MeV–GeV range. Of course, these limits are subject to the condition that DM particles with large coupling to dark photons ($\alpha_{A'} \sim \mathcal{O}(0.1)$) can be pair-produced at the LHC in significant numbers.

Looking into the future, we have also shown that LHC limits will significantly improve in Run 2

at 13 TeV center of mass energy. It is worth emphasizing here that our simplified 13 TeV analyses are still a far cry from what a full experimental search can achieve. Most importantly, with a more detailed detector simulation and data-driven background estimation methods, it will be possible to include not only muonic lepton jets, but also A' decays to electrons and hadrons.

To conclude, we have shown that lepton jets are an interesting and powerful tool to elucidate the dynamics of the dark matter sector. Together with searches for hadronic jets with non-standard properties, they will be essential in the hunt for dark matter at Run 2 of the LHC and might well be the first to find a positive signal.

Acknowledgments

It is a pleasure to thank Guido Ciapetti, Stefano Giagu, Antonio Policicchio and Christian Schmitt for very helpful discussions on the ATLAS detector and the ATLAS lepton jet analyses. We are also grateful to Torbjörn Sjöstrand for clarifying some of the subtleties of Pythia for us, and to Tilman Plehn for useful conversations in the very early stages of this project. PANM would like to thank the Mainz Institute for Theoretical Physics (MITP) for support during two visits to Mainz that were crucial for this project. JK and JL are supported by the German Research Foundation (DFG) under Grant No. KO 4820/1-1. PANM acknowledges partial support from the European Union FP7 ITN INVISIBLES (Marie Curie Actions, PITN-GA-2011-289442) and from the Spanish MINECO's "Centro de Excelencia Severo Ochoa" Programme under grant SEV-2012-0249.

-
- [1] J. Hisano, S. Matsumoto, and M. M. Nojiri, *Explosive dark matter annihilation*, *Phys.Rev.Lett.* **92** (2004) 031303, [[arXiv:hep-ph/0307216](#)].
 - [2] M. Cirelli, M. Kadastik, M. Raidal, and A. Strumia, *Model-independent implications of the e+-, anti-proton cosmic ray spectra on properties of Dark Matter*, *Nucl.Phys.* **B813** (2009) 1–21, [[arXiv:0809.2409](#)].
 - [3] N. Arkani-Hamed, D. P. Finkbeiner, T. R. Slatyer, and N. Weiner, *A Theory of Dark Matter*, *Phys.Rev.* **D79** (2009) 015014, [[arXiv:0810.0713](#)].
 - [4] D. N. Spergel and P. J. Steinhardt, *Observational evidence for selfinteracting cold dark matter*, *Phys.Rev.Lett.* **84** (2000) 3760–3763, [[arXiv:astro-ph/9909386](#)].
 - [5] S. Tulin, H.-B. Yu, and K. M. Zurek, *Beyond Collisionless Dark Matter: Particle Physics Dynamics for Dark Matter Halo Structure*, *Phys.Rev.* **D87** (2013), no. 11 115007, [[arXiv:1302.3898](#)].
 - [6] W. Shepherd, T. M. P. Tait, and G. Zaharijas, *Bound states of weakly interacting dark matter*, *Phys. Rev.* **D79** (2009) 055022, [[arXiv:0901.2125](#)].
 - [7] W. Altmannshofer, P. J. Fox, R. Harnik, G. D. Kribs, and N. Raj, *Dark Matter Signals in Dilepton Production at Hadron Colliders*, *Phys.Rev.* **D91** (2015), no. 11 115006, [[arXiv:1411.6743](#)].
 - [8] R. Foot and S. Vagnozzi, *Dissipative hidden sector dark matter*, *Phys.Rev.* **D91** (2015) 023512, [[arXiv:1409.7174](#)].
 - [9] M. Vogelsberger, S. Genel, V. Springel, P. Torrey, D. Sijacki, et al., *Properties of galaxies reproduced by a hydrodynamic simulation*, *Nature* **509** (2014) 177–182, [[arXiv:1405.1418](#)].
 - [10] T. Sawala, C. S. Frenk, A. Fattahi, J. F. Navarro, R. G. Bower, et al., *Local Group galaxies emerge from the dark*, [arXiv:1412.2748](#).
 - [11] R. Massey, L. Williams, R. Smit, M. Swinbank, T. D. Kitching, et al., *The behaviour of dark matter associated with 4 bright cluster galaxies in the 10kpc core of Abell 3827*, *Mon.Not.Roy.Astron.Soc.* **449** (2015) 3393, [[arXiv:1504.03388](#)].
 - [12] F. Kahlhoefer, K. Schmidt-Hoberg, J. Kummer, and S. Sarkar, *On the interpretation of dark matter self-interactions in Abell 3827*, [arXiv:1504.06576](#).
 - [13] B. Holdom, *Two U(1)'s and Epsilon Charge Shifts*, *Phys.Lett.* **B166** (1986) 196.
 - [14] J. Jaeckel and A. Ringwald, *The Low-Energy Frontier of Particle Physics*, *Ann.Rev.Nucl.Part.Sci.* **60** (2010) 405–437, [[arXiv:1002.0329](#)].

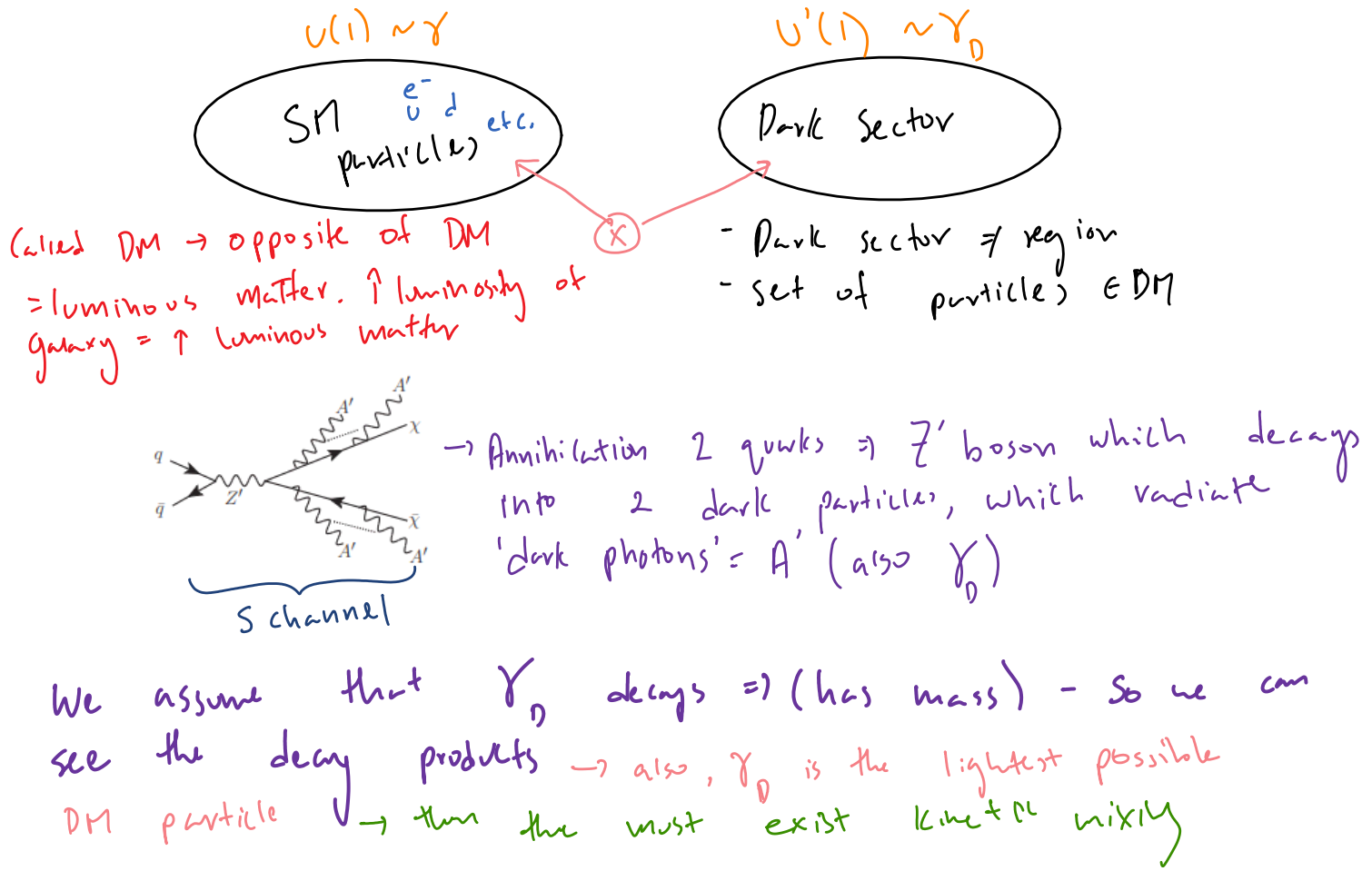
- [15] **ATLAS** Collaboration, G. Aad *et al.*, *A search for prompt lepton-jets in pp collisions at $\sqrt{s} = 7$ TeV with the ATLAS detector*, *Phys.Lett.* **B719** (2013) 299–317, [[arXiv:1212.5409](#)].
- [16] **ATLAS** Collaboration, G. Aad *et al.*, *Search for long-lived neutral particles decaying into lepton jets in proton-proton collisions at $\sqrt{s} = 8$ TeV with the ATLAS detector*, *JHEP* **1411** (2014) 088, [[arXiv:1409.0746](#)].
- [17] N. Arkani-Hamed and N. Weiner, *LHC Signals for a SuperUnified Theory of Dark Matter*, *JHEP* **0812** (2008) 104, [[arXiv:0810.0714](#)].
- [18] C. Cheung, J. T. Ruderman, L.-T. Wang, and I. Yavin, *Lepton Jets in (Supersymmetric) Electroweak Processes*, *JHEP* **1004** (2010) 116, [[arXiv:0909.0290](#)].
- [19] A. Katz and R. Sundrum, *Breaking the Dark Force*, *JHEP* **0906** (2009) 003, [[arXiv:0902.3271](#)].
- [20] Y. Bai and Z. Han, *Measuring the Dark Force at the LHC*, *Phys.Rev.Lett.* **103** (2009) 051801, [[arXiv:0902.0006](#)].
- [21] M. Baumgart, C. Cheung, J. T. Ruderman, L.-T. Wang, and I. Yavin, *Non-Abelian Dark Sectors and Their Collider Signatures*, *JHEP* **0904** (2009) 014, [[arXiv:0901.0283](#)].
- [22] Y. F. Chan, M. Low, D. E. Morrissey, and A. P. Spray, *LHC Signatures of a Minimal Supersymmetric Hidden Valley*, *JHEP* **1205** (2012) 155, [[arXiv:1112.2705](#)].
- [23] T. Han, Z. Si, K. M. Zurek, and M. J. Strassler, *Phenomenology of hidden valleys at hadron colliders*, *JHEP* **0807** (2008) 008, [[arXiv:0712.2041](#)].
- [24] A. Falkowski, J. T. Ruderman, T. Volansky, and J. Zupan, *Discovering Higgs Decays to Lepton Jets at Hadron Colliders*, *Phys.Rev.Lett.* **105** (2010) 241801, [[arXiv:1007.3496](#)].
- [25] D. Curtin, R. Essig, S. Gori, P. Jaiswal, A. Katz, *et al.*, *Exotic Decays of the 125 GeV Higgs Boson*, [arXiv:1312.4992](#).
- [26] A. Gupta, R. Primulando, and P. Saraswat, *A New Probe of Dark Sector Dynamics at the LHC*, [arXiv:1504.01385](#).
- [27] M. Autran, K. Bauer, T. Lin, and D. Whiteson, *Mono-Z': searches for dark matter in events with a resonance and missing transverse energy*, [arXiv:1504.01386](#).
- [28] Y. Bai, J. Bourbeau, and T. Lin, *Dark Matter Searches with a Mono-Z' jet*, [arXiv:1504.01395](#).
- [29] B. Batell, M. Pospelov, and A. Ritz, *Probing a Secluded U(1) at B-factories*, *Phys.Rev.* **D79** (2009) 115008, [[arXiv:0903.0363](#)].
- [30] R. Essig, P. Schuster, and N. Toro, *Probing Dark Forces and Light Hidden Sectors at Low-Energy e+e- Colliders*, *Phys.Rev.* **D80** (2009) 015003, [[arXiv:0903.3941](#)].
- [31] P. Schwaller, D. Stolarski, and A. Weiler, *Emerging Jets*, [arXiv:1502.05409](#).
- [32] T. Cohen, M. Lisanti, and H. K. Lou, *Semi-visible Jets: Dark Matter Undercover at the LHC*, [arXiv:1503.00009](#).
- [33] Y. Bai and A. Rajaraman, *Dark Matter Jets at the LHC*, [arXiv:1109.6009](#).
- [34] **ATLAS** Collaboration, G. Aad *et al.*, *Search for long-lived, weakly interacting particles that decay to displaced hadronic jets in proton-proton collisions at $\sqrt{s} = 8$ TeV with the ATLAS detector*, [arXiv:1504.03634](#).
- [35] T. Sjstrand, S. Ask, J. R. Christiansen, R. Corke, N. Desai, *et al.*, *An Introduction to PYTHIA 8.2*, [arXiv:1410.3012](#).
- [36] L. Carloni and T. Sjostrand, *Visible Effects of Invisible Hidden Valley Radiation*, *JHEP* **1009** (2010) 105, [[arXiv:1006.2911](#)].
- [37] L. Carloni, J. Rathman, and T. Sjostrand, *Discerning Secluded Sector gauge structures*, *JHEP* **1104** (2011) 091, [[arXiv:1102.3795](#)].
- [38] **ATLAS** Collaboration, G. Aad *et al.*, *Search for new phenomena in the dijet mass distribution using p – p collision data at $\sqrt{s} = 8$ TeV with the ATLAS detector*, *Phys.Rev.* **D91** (2015), no. 5 052007, [[arXiv:1407.1376](#)].
- [39] **CMS** Collaboration, V. Khachatryan *et al.*, *Search for resonances and quantum black holes using dijet mass spectra in proton-proton collisions at $\sqrt{s} = 8$ TeV*, *Phys.Rev.* **D91** (2015), no. 5 052009, [[arXiv:1501.04198](#)].
- [40] **CDF** Collaboration, T. Aaltonen *et al.*, *Search for new particles decaying into dijets in proton-antiproton collisions at $s^{**}(1/2) = 1.96$ -TeV*, *Phys.Rev.* **D79** (2009) 112002, [[arXiv:0812.4036](#)].
- [41] **ATLAS** Collaboration, G. Aad *et al.*, *Search for new phenomena in final states with an energetic jet and large missing transverse momentum in pp collisions at $\sqrt{s} = 8$ TeV with the ATLAS detector*, [arXiv:1502.01518](#).
- [42] **CMS Collaboration** Collaboration, V. Khachatryan *et al.*, *Search for dark matter, extra*

- dimensions, and unparticles in monojet events in proton-proton collisions at $\sqrt{s} = 8$ TeV,* [arXiv:1408.3583](#).
- [43] J. Liu, N. Weiner, and W. Xue, *Signals of a Light Dark Force in the Galactic Center*, [arXiv:1412.1485](#).
- [44] J.-M. Zheng, Z.-H. Yu, J.-W. Shao, X.-J. Bi, Z. Li, and H.-H. Zhang, *Constraining the interaction strength between dark matter and visible matter: I. fermionic dark matter*, *Nucl. Phys.* **B854** (2012) 350–374, [[arXiv:1012.2022](#)].
- [45] H. Dreiner, M. Huck, M. Kr?mer, D. Schmeier, and J. Tattersall, *Illuminating Dark Matter at the ILC*, *Phys. Rev.* **D87** (2013), no. 7 075015, [[arXiv:1211.2254](#)].
- [46] R. T. D’Agnolo and J. T. Ruderman, *Forbidden Dark Matter*, [arXiv:1505.07107](#).
- [47] K. Petraki, L. Pearce, and A. Kusenko, *Self-interacting asymmetric dark matter coupled to a light massive dark photon*, *JCAP* **1407** (2014) 039, [[arXiv:1403.1077](#)].
- [48] SuperCDMS Collaboration, R. Agnese *et al.*, *Search for Low-Mass Weakly Interacting Massive Particles Using Voltage-Assisted Calorimetric Ionization Detection in the SuperCDMS Experiment*, *Phys. Rev. Lett.* **112** (2014), no. 4 041302, [[arXiv:1309.3259](#)].
- [49] S. W. Randall, M. Markevitch, D. Clowe, A. H. Gonzalez, and M. Bradac, *Constraints on the Self-Interaction Cross-Section of Dark Matter from Numerical Simulations of the Merging Galaxy Cluster 1E 0657-56*, *Astrophys. J.* **679** (2008) 1173–1180, [[arXiv:0704.0261](#)].
- [50] A. H. Peter, M. Rocha, J. S. Bullock, and M. Kaplinghat, *Cosmological Simulations with Self-Interacting Dark Matter II: Halo Shapes vs. Observations*, *Mon. Not. Roy. Astron. Soc.* **430** (2013) 105, [[arXiv:1208.3026](#)].
- [51] M. R. Whalley, *A compilation of data on hadronic total cross sections in e^+e^- interactions*, *Journal of Physics G: Nuclear and Particle Physics* **29** (2003), no. 12A A1.
- [52] “Hepdata on-line data review.” <http://hepdata.cedar.ac.uk/review/rsig/>.
- [53] T. Plehn, *Lectures on LHC Physics*, *Lect. Notes Phys.* **844** (2012) 1–193, [[arXiv:0910.4182](#)].
- [54] P. Ciafaloni, D. Comelli, A. Riotto, F. Sala, A. Strumia, *et al.*, *Weak Corrections are Relevant for Dark Matter Indirect Detection*, *JCAP* **1103** (2011) 019, [[arXiv:1009.0224](#)].
- [55] J. C. Collins, D. E. Soper, and G. F. Sterman, *Factorization of Hard Processes in QCD*, *Adv. Ser. Direct. High Energy Phys.* **5** (1988) 1–91, [[arXiv:hep-ph/0409313](#)].
- [56] S. Catani, S. Dittmaier, M. H. Seymour, and Z. Trocsanyi, *The Dipole formalism for next-to-leading order QCD calculations with massive partons*, *Nucl. Phys.* **B627** (2002) 189–265, [[arXiv:hep-ph/0201036](#)].
- [57] A. Arbuzov, *Nonsinglet splitting functions in QED*, *Phys. Lett.* **B470** (1999) 252–258, [[arXiv:hep-ph/9908361](#)].
- [58] G. Arfken and H. Weber, *Mathematical methods for physicists*. Elsevier Acad. Press, 2008.
- [59] J. W. Cooley and J. W. Tukey, *An algorithm for the machine calculation of complex fourier series*, *Math. Comput.* **19** (1965) 297–301.
- [60] A. Belyaev, N. D. Christensen, and A. Pukhov, *CalcHEP 3.4 for collider physics within and beyond the Standard Model*, *Comput. Phys. Commun.* **184** (2013) 1729–1769, [[arXiv:1207.6082](#)].
- [61] J. M. Campbell, R. K. Ellis, and W. T. Giele, *A Multi-Threaded Version of MCFM*, *Eur. Phys. J.* **C75** (2015), no. 6 246, [[arXiv:1503.06182](#)].
- [62] M. Cacciari, G. P. Salam, and G. Soyez, *The Anti- $k(t)$ jet clustering algorithm*, *JHEP* **0804** (2008) 063, [[arXiv:0802.1189](#)].
- [63] M. Cacciari, G. P. Salam, and G. Soyez, *FastJet User Manual*, *Eur. Phys. J.* **C72** (2012) 1896, [[arXiv:1111.6097](#)].
- [64] Particle Data Group Collaboration, K. Olive *et al.*, *Review of Particle Physics*, *Chin. Phys.* **C38** (2014) 090001.
- [65] A. L. Read, *Presentation of search results: The $CL(s)$ technique*, *J. Phys.* **G28** (2002) 2693–2704.
- [66] M. Pospelov, *Secluded U(1) below the weak scale*, *Phys. Rev.* **D80** (2009) 095002, [[arXiv:0811.1030](#)].
- [67] H. Davoudiasl, H.-S. Lee, and W. J. Marciano, *Dark Side of Higgs Diphoton Decays and Muon $g-2$* , *Phys. Rev.* **D86** (2012) 095009, [[arXiv:1208.2973](#)].
- [68] M. Endo, K. Hamaguchi, and G. Mishima, *Constraints on Hidden Photon Models from Electron $g-2$ and Hydrogen Spectroscopy*, *Phys. Rev.* **D86** (2012) 095029, [[arXiv:1209.2558](#)].
- [69] HADES Collaboration, G. Agakishiev *et al.*, *Searching a Dark Photon with HADES*, *Phys. Lett.* **B731** (2014) 265–271, [[arXiv:1311.0216](#)].
- [70] KLOE-2 Collaboration, D. Babusci *et al.*, *Limit on the production of a light vector gauge boson in phi meson decays with the KLOE detector*, *Phys. Lett.* **B720** (2013) 111–115, [[arXiv:1210.3927](#)].

- [71] **KLOE-2** Collaboration, D. Babusci *et al.*, *Search for light vector boson production in $e^+e^- \rightarrow \mu^+\mu^-\gamma$ interactions with the KLOE experiment*, *Phys.Lett.* **B736** (2014) 459–464, [[arXiv:1404.7772](#)].
- [72] **APEX** Collaboration, S. Abrahamyan *et al.*, *Search for a New Gauge Boson in Electron-Nucleus Fixed-Target Scattering by the APEX Experiment*, *Phys.Rev.Lett.* **107** (2011) 191804, [[arXiv:1108.2750](#)].
- [73] **BaBar** Collaboration, B. Aubert *et al.*, *Search for Dimuon Decays of a Light Scalar Boson in Radiative Transitions Upsilon —> gamma A0*, *Phys. Rev. Lett.* **103** (2009) 081803, [[arXiv:0905.4539](#)].
- [74] **BaBar** Collaboration, J. Lees *et al.*, *Search for a Dark Photon in e^+e^- Collisions at BaBar*, *Phys.Rev.Lett.* **113** (2014), no. 20 201801, [[arXiv:1406.2980](#)].
- [75] J. Blümlein and J. Brunner, *New Exclusion Limits for Dark Gauge Forces from Beam-Dump Data*, *Phys.Lett.* **B701** (2011) 155–159, [[arXiv:1104.2747](#)].
- [76] J. D. Bjorken, R. Essig, P. Schuster, and N. Toro, *New Fixed-Target Experiments to Search for Dark Gauge Forces*, *Phys.Rev.* **D80** (2009) 075018, [[arXiv:0906.0580](#)].
- [77] A. Bross, M. Crisler, S. H. Pordes, J. Volk, S. Errede, *et al.*, *A Search for Shortlived Particles Produced in an Electron Beam Dump*, *Phys.Rev.Lett.* **67** (1991) 2942–2945.
- [78] **A1** Collaboration, H. Merkel *et al.*, *Search for Light Gauge Bosons of the Dark Sector at the Mainz Microtron*, *Phys.Rev.Lett.* **106** (2011) 251802, [[arXiv:1101.4091](#)].
- [79] M. Davier and H. Nguyen Ngoc, *An Unambiguous Search for a Light Higgs Boson*, *Phys.Lett.* **B229** (1989) 150.
- [80] J. Blümlein and J. Brunner, *New Exclusion Limits on Dark Gauge Forces from Proton Bremsstrahlung in Beam-Dump Data*, *Phys.Lett.* **B731** (2014) 320–326, [[arXiv:1311.3870](#)].
- [81] S. Gnenienko, *Constraints on sub-GeV hidden sector gauge bosons from a search for heavy neutrino decays*, *Phys.Lett.* **B713** (2012) 244–248, [[arXiv:1204.3583](#)].
- [82] R. Essig, R. Harnik, J. Kaplan, and N. Toro, *Discovering New Light States at Neutrino Experiments*, *Phys.Rev.* **D82** (2010) 113008, [[arXiv:1008.0636](#)].
- [83] J. B. Dent, F. Ferrer, and L. M. Krauss, *Constraints on Light Hidden Sector Gauge Bosons from Supernova Cooling*, [arXiv:1201.2683](#).
- [84] H. K. Dreiner, J.-F. Fortin, C. Hanhart, and L. Ubaldi, *Supernova constraints on MeV dark sectors from e^+e^- annihilations*, *Phys.Rev.* **D89** (2014), no. 10 105015, [[arXiv:1310.3826](#)].
- [85] **CERN NA48/2** Collaboration, *Search for the dark photon in π^0 decays*, [arXiv:1504.00607](#).

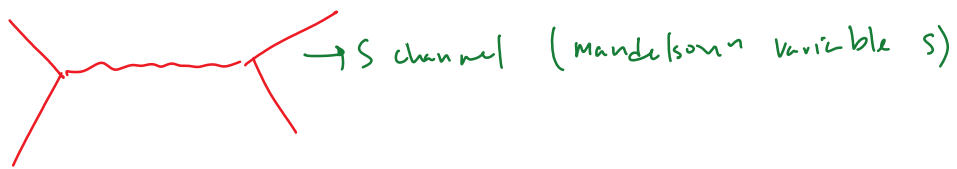
Dark Matter

Wednesday, October 27, 2021 2:15 PM



S Channel Diagrams

Wednesday, October 27, 2021 2:18 PM

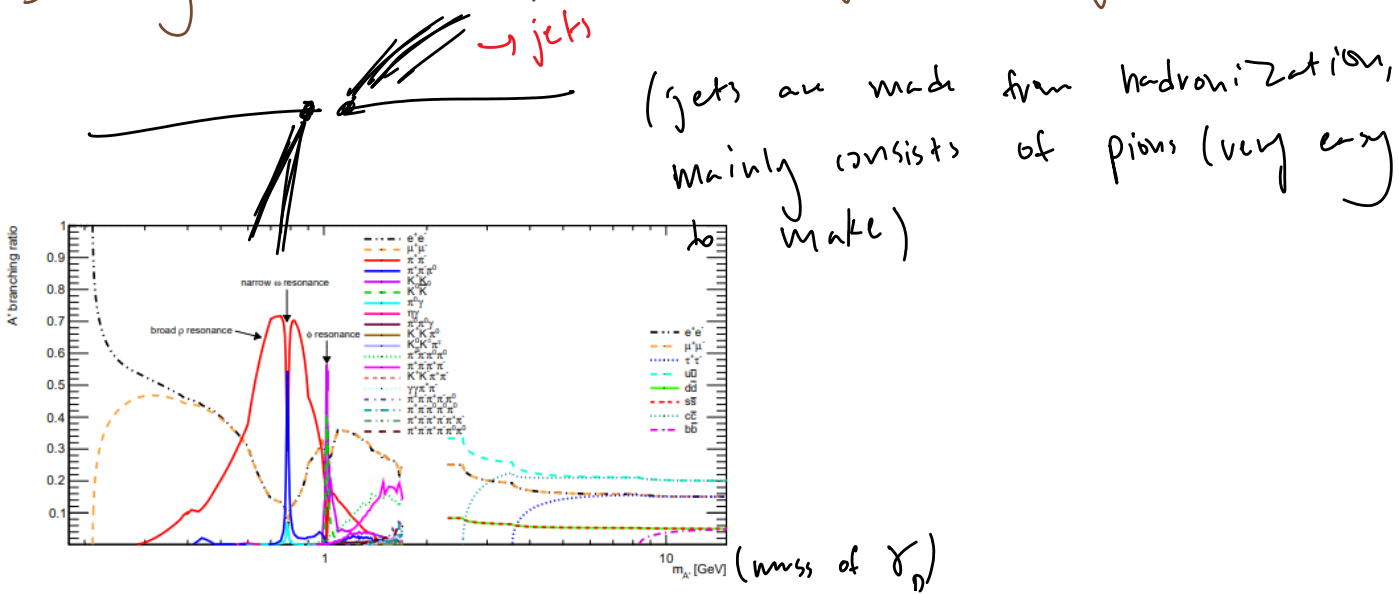


Branching ratio

Wednesday, October 27, 2021 2:32 PM

$$\gamma_D \rightarrow e^- e^+; \rightarrow \mu^- \mu^+; \pi^+ \pi^-; \pi^+ \pi^- \pi^0$$

Branching ratio: percentage of each type of decay



General QCD diagram



The idea is that looking for the leptons from γ_D decays helps us understand what they are, if \exists .

Decays...

Wednesday, September 14, 2022 11:34 AM

Neutralinos can decay to X particle + dark photon

Heavy dark higgs + 2 dark ph

Pseudo scalar higgs + darkphotons

Light dark higgs + ME (missing energy)

Assumed that the sum of SUSy particles masses = sum of neutralinos (or some generic WIMP)

Introduction 12/1

Wednesday, November 10, 2021 2:10 PM

Standard Model Review

Symmetry $SU(3) \times SU(2) \times U(1)$

Helicity

- Particles spin, and moves
- If particle is a fermion, only two ways to spin - Right handed / Left handed
- Which way it is spinning relative to its velocity
- Weak force only interacts with left handed particles
- All neutrinos are left handed
- Interacts with right handed antiparticles, and left handed antineutrinos
- Sterile neutrinos do not interact (right handed neutrinos, or left handed anti neutrinos)
- Existence of right handed weak force? - Right handed counter particles (W' and Z')
 - o Same as left right symmetry
 - o One of the results of doubly charged higgs

Higgs mechanism

- Spontaneous electroweak symmetry breaking
- Single theory describing weak and electromagnetism
- Exists a symmetry break between weak and electromagnetism
- Mathematical mechanism to explain the break
- Causes the Z and W bosons to have mass
- Not an event - a thing that happens - a mathematical model

Doubly Charged Higgs

Left - right symmetry

Doubly Charged Higgs predictions

Event Signature

Current Limits

.

Dark Photons

Dark Matter

Dark sector/hidden valley

Kinetic mixing

Dark radiation - DUE 11/28 AT 11:59

Current Limits

Lepton jets